

# An improved carbon dioxide snow spectral albedo model: Application to Martian conditions

D. Singh<sup>1</sup>, and M.G. Flanner<sup>1</sup>

<sup>1</sup>Climate and Space Sciences and Engineering, University of Michigan, Ann Arbor, Michigan, USA

Corresponding author: Deepak Singh (sdeepak@umich.edu)

## Key Points:

- We extend an Earth-based H<sub>2</sub>O snow model to simulate CO<sub>2</sub> snow albedo
- Improved CO<sub>2</sub> ice refractive indices produce very high (~0.96) CO<sub>2</sub> snow albedo
- we explore a range of conditions applicable to Mars and evaluate the model against measurements

This is the author manuscript accepted for publication and has undergone full peer review but has not been through the copyediting, typesetting, pagination and proofreading process, which may lead to differences between this version and the [Version of Record](#). Please cite this article as doi: [10.1002/2016JE005040](https://doi.org/10.1002/2016JE005040)

## Abstract

Carbon dioxide ice is abundant on the Martian surface, and plays an important role in the planet's energy budget due to its high reflectivity and seasonal variation. Here, we adapt the terrestrial Snow, Ice, and Aerosol Radiation (SNICAR) model to simulate CO<sub>2</sub> snow albedo across the ultraviolet, visible, and near-IR spectrum (0.2-5.0 μm). We apply recent laboratory derived refractive indices of CO<sub>2</sub> ice, which produce higher broadband CO<sub>2</sub> snow albedo (0.93–0.98) than previously estimated. Compared with H<sub>2</sub>O snow, we find that CO<sub>2</sub> snow albedo is much higher in the near-IR spectrum, less dependent on ice grain size, less dependent on solar zenith angle, and more susceptible to darkening from dust. A mass concentration of 0.01% Martian dust reduces visible and near-IR CO<sub>2</sub> snow albedos by about 60% and 35%, respectively. The presence of small amounts of H<sub>2</sub>O snow on top of CO<sub>2</sub> snow can substantially decrease the surface albedo. Whereas 2.5 cm of H<sub>2</sub>O snow can completely mask the impact of underlying CO<sub>2</sub> ice or the surface, roughly twice as much overlying CO<sub>2</sub> snow is required to mask underlying H<sub>2</sub>O snow. Similarly, a 10% mixing ratio of H<sub>2</sub>O ice embedded in CO<sub>2</sub> snow decreases broadband albedo by 0.18, while 10% CO<sub>2</sub> ice elevates H<sub>2</sub>O snow broadband albedo by 0.10. We also present comparisons between hemispherical albedo produced by SNICAR and observations of directional reflectance of Martian polar ice caps. While imperfect, this best-fit analysis provides general ranges of physical parameters in different Martian environments that produce reasonable model–observation agreement.

## 1 Introduction

The Martian atmosphere consists primarily of carbon dioxide, and Martian polar caps are covered primarily with carbon dioxide ice [Leighton and Murray, 1966; Herr and Pimentel, 1969; Larson and Fink, 1972; Forget, 1998; Bibring et al., 2005]. H<sub>2</sub>O ice is also present at the surface of the perennial ice caps, with small amounts of seasonal deposition in other parts

of the planet [e.g., *Kieffer et al.*, 2000; *Bibring et al.*, 2004; *Brown et al.*, 2014]. Significant portions of atmospheric CO<sub>2</sub> (25-30%) deposit seasonally in each hemisphere, as indicated by model simulations and surface pressure measurements [*Tillman et al.*, 1993; *Forget et al.*, 1998; *Kieffer and Titus*, 2001]. To understand the impact of these ices on the planet's cryosphere albedo, it is important to accurately determine the spectral dependence of CO<sub>2</sub> snow albedo and influences of properties such as dust content, ice grain size, and snow thickness, as well as the albedo effects of mixing and layering of CO<sub>2</sub> and H<sub>2</sub>O snow.

Our work determines the albedo of CO<sub>2</sub> snow by extending the Earth-based Snow, Ice, and Aerosol Radiation (SNICAR) model [*Flanner et al.*, 2007; *Flanner et al.*, 2009], originally designed for H<sub>2</sub>O snow. SNICAR utilizes the multiple scattering, multi-layer two-stream radiative approximation described by *Toon et al.* [1989], with the delta-hemispheric mean approximation. We extend the current version of SNICAR from 470 bands (over the wavelength range 0.3-5.0 μm) to 480 bands spanning 0.2-5.0 μm at 10 nm spectral resolution. We include these extra 10 bands in the ultraviolet (UV) spectrum because of the lack of ozone in the Martian atmosphere compared to Earth [*Montmessin and Lefèvre*, 2013], meaning more UV radiation reaches the Martian surface and interacts with snow. A single-layer implementation of SNICAR can be operated interactively on the web at: <http://snow.engin.umich.edu>.

Very few studies have focused on modeling of Martian CO<sub>2</sub> snow albedo across the UV, visible and near-IR spectrum [*Warren et al.*, 1990; *Hansen*, 1999; *Bonev et al.*, 2008]. *Langevin et al.*, [2007] and *Appéré et al.*, [2011] present modeled near-IR albedo of Martian cryospheric surfaces, as discussed in Section 4. With the availability of more accurate and spectrally resolved laboratory measurements of CO<sub>2</sub> ice complex refractive indices across the solar spectrum [*Hansen*, 1997; *Hansen* 2005], we provide improved and updated spectral albedos of carbon dioxide snow with applicability to Martian conditions. The presence of light-absorbing impurities generally lowers snow albedo. We simulate the impact of Martian dust [*Wolff et al.*, 2006; *Wolff et al.*, 2009; *Wolff et al.*, 2010] and palagonite [*Clark et al.*, 1990; *Clancy et al.*, 1995] on surface cryosphere albedo. Palagonite is a volcanic rock and serves as a terrestrial analog for Martian dust [*Banin et al.*, 1997]. We perform multiple

analyses to determine the sensitivity of cryosphere spectral albedo to the amount and type of dust, presence of both ices, ice grain size, snow layer thickness, and solar zenith angle. We also compare our simulations with observed Mars surface albedo derived from Compact Reconnaissance Imaging Spectrometer (CRISM) measurements, and the OMEGA instrument [Appéré *et al.*, 2011] (section 4). Apparent albedo, derived by Brown *et al* [2014] using CRISM measurements, were provided by Adrian Brown (SETI Institute, personal communication), and observations and modeled albedo from the OMEGA instrument were provided by Thomas Appéré (IPAG, Grenoble, personal communication).

## 2 Data and methodology

Hansen [1997, 2005] made extensive laboratory measurements of the complex refractive indices of solid CO<sub>2</sub> ice in the spectral range from 0.174 μm to 333 μm. We apply these data along with Mie calculations to derive optical properties of different lognormal size distributions of CO<sub>2</sub> ice particles, reported with effective radius ( $r_{eff}$ ), or the surface area-weighted mean radius of the size distribution. Our simulations of H<sub>2</sub>O snow albedo utilize refractive indices of H<sub>2</sub>O ice provided by Warren and Brandt [2008]. We use “central hematite” dust mineral fractions from Balkanski *et al.* [2007] as a proxy of typical Earth dust. These mineral abundances are representative of aeolian dust from the Saharan desert. Refractive indices for this dust mixture are derived using the Maxwell-Garnett mixing approximation, following e.g., Sokolik and Toon [1999], along with measurements of mineral refractive indices from various sources. Refractive indices of Martian dust (hereafter Mars dust) were provided by Mike Wolff (Space Science Institute, personal communication), and were derived using data from instruments onboard the Mars Reconnaissance Orbiter (MRO), as described by Wolff *et al.* [2009], and Wolff *et al.* [2010]. We combine refractive indices of palagonite from Clark *et al.* [1990] over the 0.2 μm to 0.6 μm spectral range and measurements from 0.6 μm to 5 μm made by Clancy *et al.* [1995] to derive data over the

solar spectrum. In this study, we divide our broadband (0.2-5.0  $\mu\text{m}$ ) into two sub-regions: Visible (0.2-0.7  $\mu\text{m}$ ) and near-IR (0.7-5.0  $\mu\text{m}$ ).

We determine the spectrally-varying single scatter albedo ( $\omega_0$ ), scattering asymmetry parameter ( $g$ ), and mass extinction cross-section for all three dust types using Mie Theory with an assumed gamma size distribution [Hansen and Travis, 1974] with  $r_{\text{eff}}=1.5\mu\text{m}$  and effective variance ( $v_{\text{eff}}=0.3$ ) [Wolff et al., 2006]. Figure 1 shows the optical properties for these dust types. Mass absorption cross-section (Fig. 1d) is the product of single scatter albedo (Fig. 1a) and mass extinction cross-section (Fig 1b). We assume the same dust density of  $2000\text{ kg/m}^3$  for both palagonite and Mars dust [Stronck and Schmincke, 2002], and a dust density of  $2570\text{ kg/m}^3$  for Earth dust, based on the volume fraction-weighted densities of the constituent minerals [Balkanski et al., 2007].

The bulk optical properties (extinction optical depth ( $\tau$ ),  $\omega_0$ , and  $g$ ) for each snow layer are calculated from the abundances of each constituent [e.g., Flanner et al, 2007], with  $\tau$  calculated as the sum of that associated with each constituent,  $\omega_0$  as a  $\tau$ -weighted average of each constituent, and  $g$  as a scattering optical depth (product of  $\tau$  and  $\omega_0$ ) weighted average of the asymmetry parameter of each constituent. These bulk layer properties are then applied in the two stream multiple scattering approximation adopted by SNICAR. We utilize this extended framework of SNICAR to first simulate the albedo of pure  $\text{CO}_2$  snow across the visible and near-IR spectrum. We then explore and compare the impacts of Earth dust, Mars dust and palagonite on  $\text{CO}_2$  and  $\text{H}_2\text{O}$  snow albedo. Finally, we adopt a two layer model (with the bottom layer being semi-infinite) to calculate the impacts of  $\text{H}_2\text{O}$  snow presence on top of  $\text{CO}_2$  snow and vice-versa. In all other cases we assume only a single snow layer, either with semi-infinite thickness or varying shallow thicknesses. Here, a layer with thickness of 100 m is referred to as semi-infinite. Figure 2 shows simplified diagrams of the various model configurations applied in this paper.

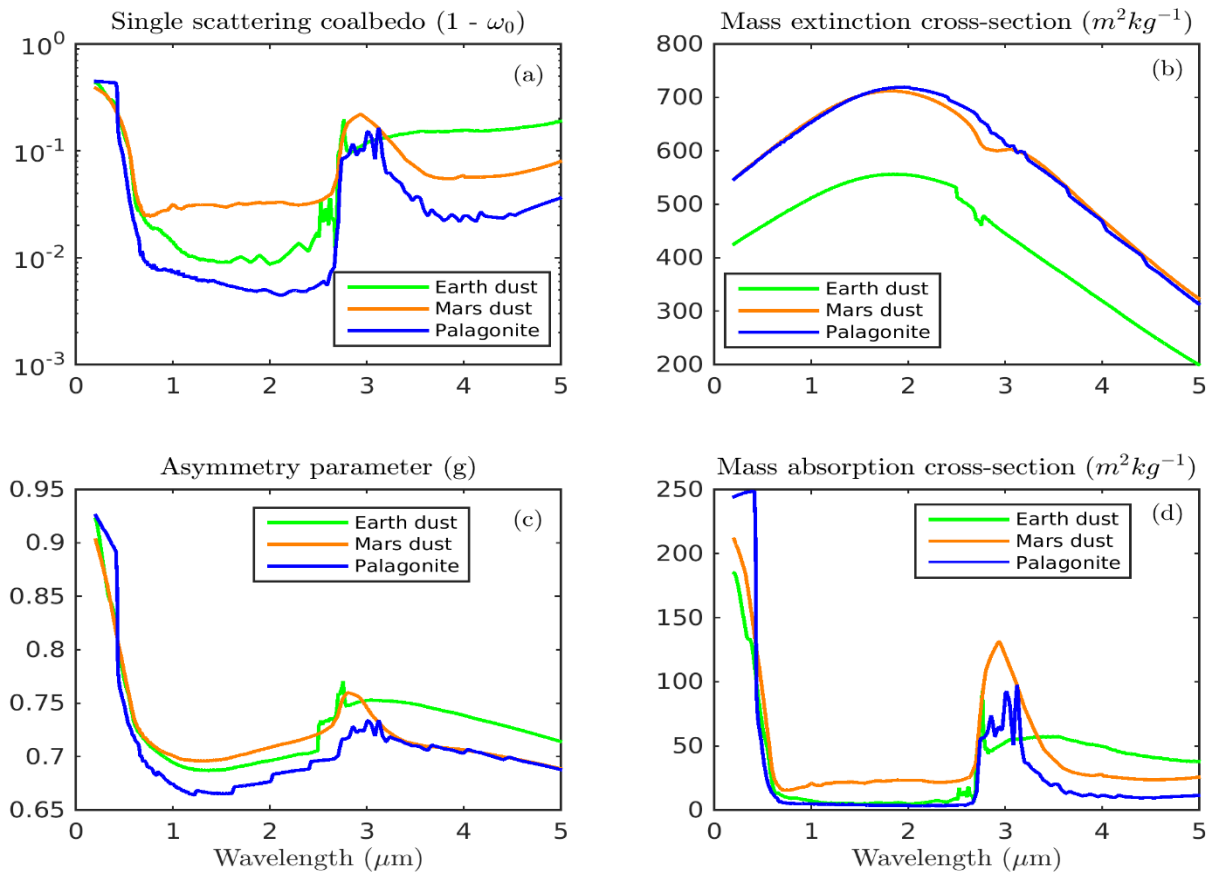


Figure 1: Spectral optical properties of the Earth dust, Martian dust, and palagonite applied in this study.

Author Me

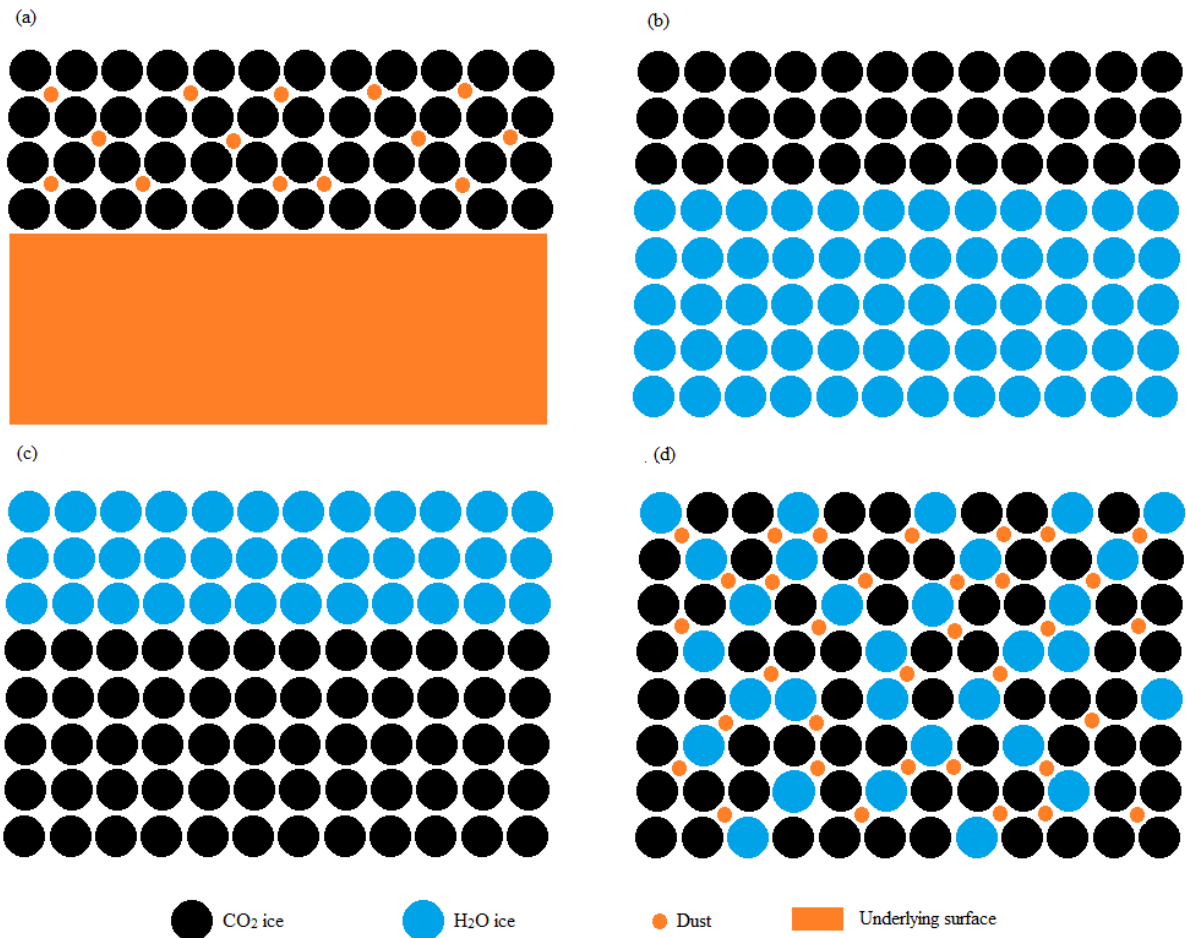


Figure 2. Schematic of the various model configurations applied in this paper: (a) a single CO<sub>2</sub> or H<sub>2</sub>O snow layer (with dust) on top of solid underlying surface; (b) CO<sub>2</sub> snow with variable thickness on top of a semi-infinite H<sub>2</sub>O snow layer; (c) H<sub>2</sub>O snow with variable thickness on top of a semi-infinite CO<sub>2</sub> snow layer; (d) mixed snow layers with dust.

### 3 Results

Figure 3 shows the spectral hemispheric albedo of pure, semi-infinite CO<sub>2</sub> and H<sub>2</sub>O snow with spherical grain effective radius of 100 μm and solar zenith angle of 60°. It is evident that the CO<sub>2</sub> is more reflective than H<sub>2</sub>O snow, especially in the near-IR spectrum. Table 1 compares solar broadband, visible and near-IR albedo for both types of snow, where band-averaged values are weighted with solar spectral irradiance measurements from *Labs and Neckel* [1968]. H<sub>2</sub>O snow albedo is only about two-thirds of the CO<sub>2</sub> snow albedo in the near-

IR spectrum, although this ratio is grain size dependent (section 3.2). With the presence of both CO<sub>2</sub> and H<sub>2</sub>O ices on Martian polar caps, the contrasting reflectivity of these types of snow could significantly impact planetary shortwave energy fluxes, both at the surface and top of atmosphere.

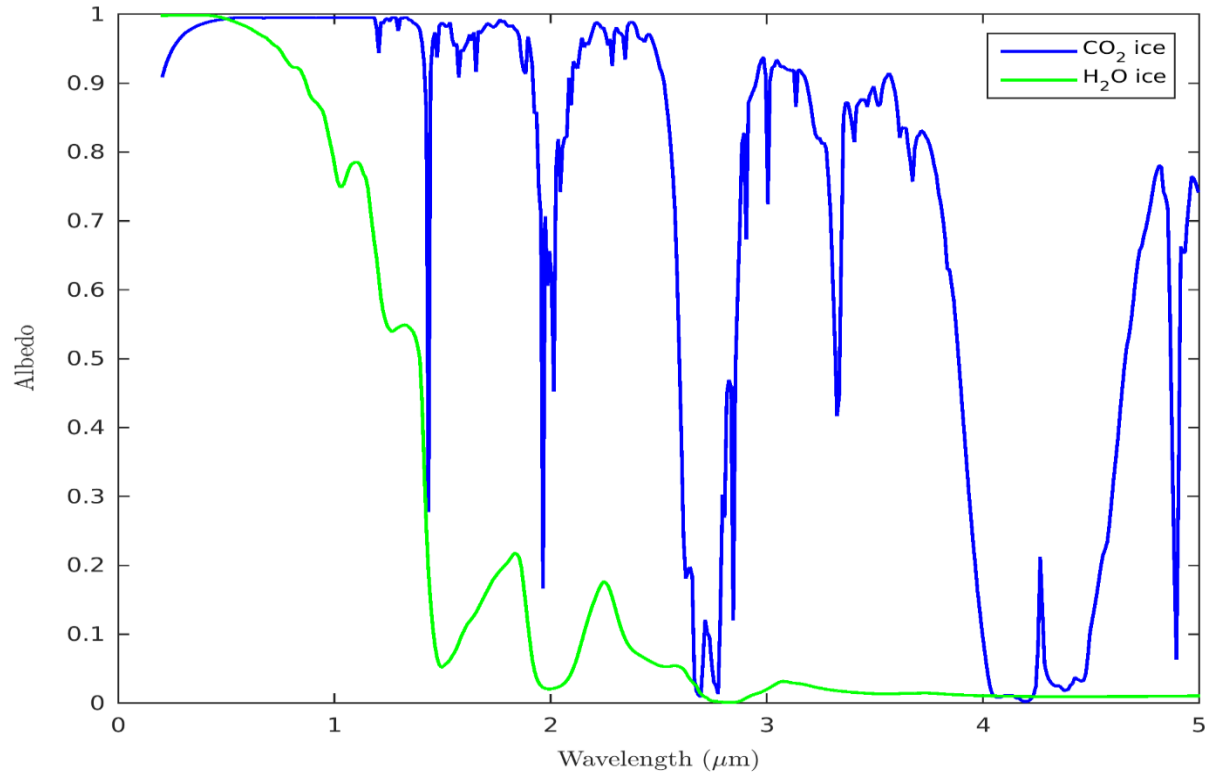


Figure 3. Comparison of CO<sub>2</sub> and H<sub>2</sub>O snow spectral albedo simulated with the SNICAR model (Grain size = 100 μm and solar zenith angle = 60°)

Table 1: Albedo values for pure, semi-infinite CO<sub>2</sub> and H<sub>2</sub>O snow in different spectral bands (Grain size = 100 μm and solar zenith angle = 60°)

	pure CO <sub>2</sub>	pure H <sub>2</sub> O
<b>Visible (0.2-0.7 μm)</b>	0.991	0.988
<b>Near-IR (0.7-5.0 μm)</b>	0.952	0.609
<b>Broadband (0.2-5.0 μm)</b>	0.970	0.787

Snow albedo depends on many physical quantities, including grain size, solar zenith angle, layer thickness, and type and amount of impurities. We performed a sensitivity analysis to



understand the effect of these parameters on carbon dioxide snow albedo, and describe this analysis below. We assume an effective grain size of  $100\ \mu\text{m}$  and solar zenith angle of  $60^\circ$  for all analyses, unless stated otherwise. For comparing  $\text{CO}_2$  and  $\text{H}_2\text{O}$  albedo, we also assume identical pore volume fractions for each type of ice. A typical bulk density of settled snow on Earth is  $200\ \text{kg/m}^3$  (e.g., *EN 1991-1-3*). Because the bulk densities of  $\text{H}_2\text{O}$  and  $\text{CO}_2$  ice are assumed to be  $917\ \text{kg/m}^3$  and  $1500\ \text{kg/m}^3$ , respectively, we therefore assume  $\text{H}_2\text{O}$  and  $\text{CO}_2$  snow densities of  $200\ \text{kg/m}^3$  and  $327.15 (= 200 \times 1500 / 917)\ \text{kg/m}^3$ , respectively.

### 3.1 Solar zenith angle

We see little effect of solar zenith angle on  $\text{CO}_2$  snow albedo (Fig. 4). The broadband albedo only changes from 0.98 to 0.96 over the  $80^\circ$  change in zenith angle. This compares with  $\text{H}_2\text{O}$  snow albedo, which varies from 0.75 to 0.82 for the same set of parameters. Variability in albedo with solar zenith angle is greater in more absorptive parts of the spectrum (i.e., the near-IR), but for  $\text{CO}_2$  snow the variability is small in the parts of the spectrum containing most of the solar energy.

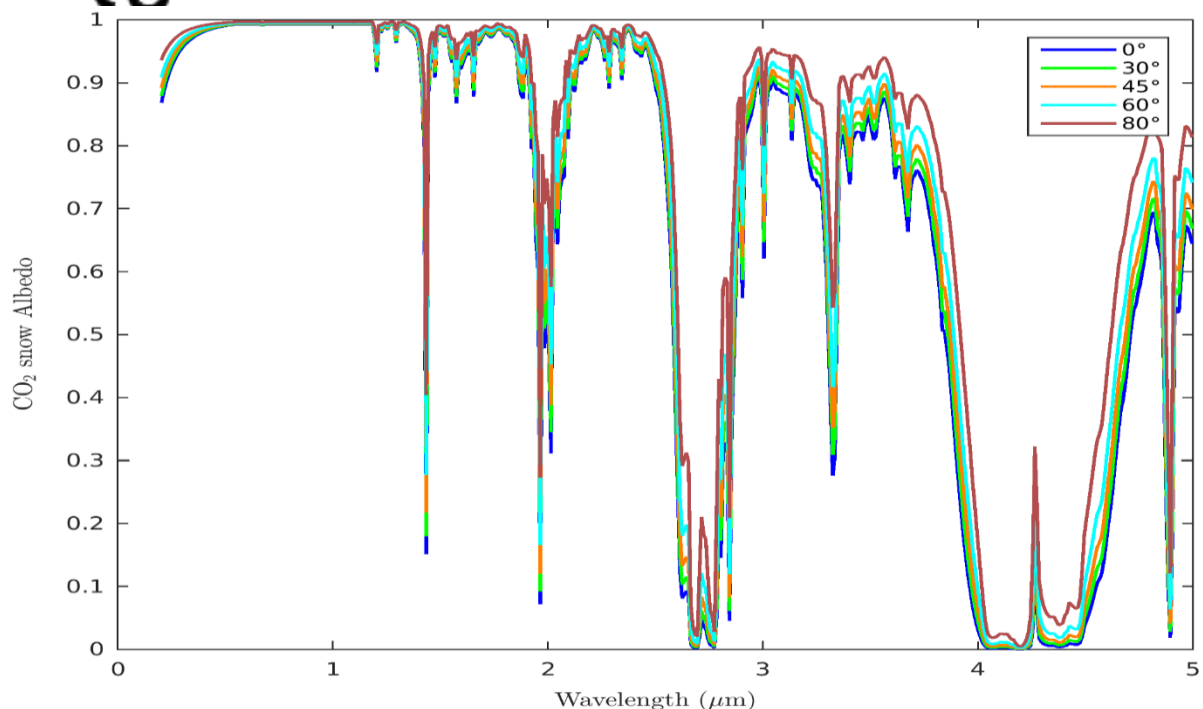


Figure 4: Variation of CO<sub>2</sub> snow albedo with solar zenith angle

### 3.2 Grain Size

We simulate a monotonic decrease in snow albedo with increasing effective grain size (Fig. 5). With larger grain size, ice volume per surface area increases, resulting in greater absorption of light, as also occurs with H<sub>2</sub>O snow [e.g., *Wiscombe and Warren, 1980*]. The broadband (near-IR) albedo of CO<sub>2</sub> snow drops from 0.98 to 0.93 (0.96 to 0.89) for grain size increasing from 50  $\mu\text{m}$  to 1500  $\mu\text{m}$ . This is also smaller variability than exhibited by H<sub>2</sub>O snow, whose broadband (near-IR) albedo changes from 0.82 to 0.65 (0.66 to 0.37) over the same range in effective grain size. CO<sub>2</sub> snow albedo varies less with grain size because CO<sub>2</sub> ice is inherently less absorptive in the near-IR than H<sub>2</sub>O ice. Consequently the incremental increase in absorption associated with increasing photon path length within larger ice grains is smaller for CO<sub>2</sub> snow than H<sub>2</sub>O snow.

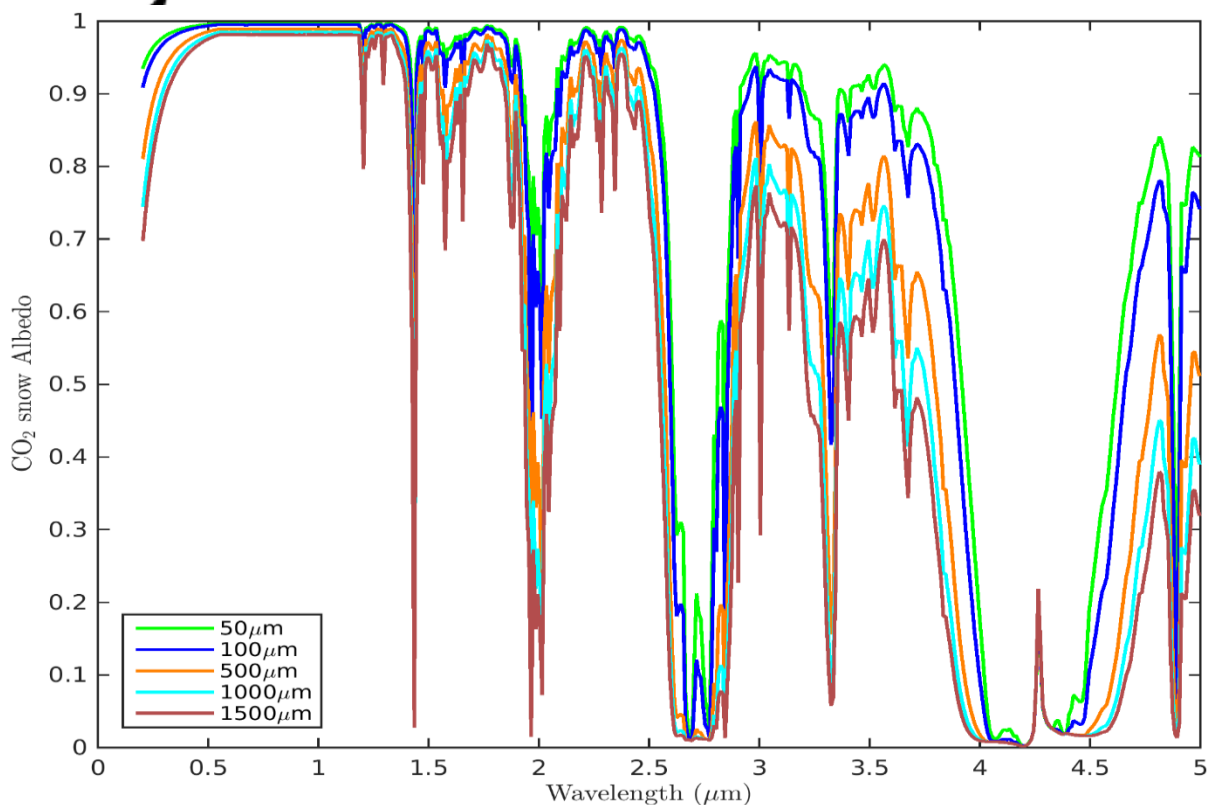


Figure 5: Variation of CO<sub>2</sub> snow albedo with effective grain radius

### 3.3 Snow thickness

Figure 6 shows the combined impacts of snow thickness and grain size on CO<sub>2</sub> and H<sub>2</sub>O broadband snow albedo, for snow overlying a surface with spectrally constant albedo of 0.2 (model configuration shown in Fig. 2a). For a given grain size, CO<sub>2</sub> snow albedo has a larger variation over the entire thickness range compared to H<sub>2</sub>O snow albedo. CO<sub>2</sub> snow albedo is almost independent of grain size when the snow layer is thick, and consequently all curves saturate at a similarly high albedo ranging from 0.93-0.98. However, H<sub>2</sub>O snow albedo has greater dependence on grain size, as each curve saturates at a different albedo ranging from 0.65-0.82.

We define “saturation thickness” as the snow thickness needed for the broadband albedo to differ by less than 0.01 from its semi-infinite value. Once the snow layer thickness exceeds the saturation thickness, the impact of the underlying surface becomes negligible as an insignificant amount of light penetrates through the snow to interact with the underlying surface. We note, however, that the penetration depth of radiation in snow depends strongly on wavelength, with multiple scattering leading to much deeper penetration and influence of underlying substrate at wavelengths where the ice absorbs weakly [e.g., *Wiscombe and Warren, 1980*]. The saturation thickness also depends on snow density, with higher density producing lower saturation thickness. Table 2 presents the saturation thickness required for different grain sizes for both types of snow. The saturation thickness is grain size-dependent, increasing from about 6 to 100 cm, and from about 5 to 83 cm as grain size increases from 50 to 1500  $\mu\text{m}$  for CO<sub>2</sub> and H<sub>2</sub>O snow, respectively. With other factors equal, CO<sub>2</sub> snow has higher saturation thickness than H<sub>2</sub>O snow because CO<sub>2</sub> ice is less absorptive than H<sub>2</sub>O ice, especially in the near-IR region, enabling multiple-scattered photons to penetrate deeper in the snow. Also the difference in saturation thicknesses increases with larger grain size because of less dependency of CO<sub>2</sub> snow albedo on grain size compared to H<sub>2</sub>O snow (section 3.2). Finally, we note that studies on optical properties of ice particles have found that the scattering asymmetry parameter is generally smaller for non-spherical ice particles than equal volume/area ice spheres [e.g., *Fu, 2007; Libois et al., 2013; Räisänen et al., 2015*]. An implication of this is that saturation thickness will be smaller for non-spherical ice

particles than values reported here, as photons are scattered less preferentially into the forward direction.

Table 2: Saturation snow layer thickness with various grain sizes for each type of snow. CO<sub>2</sub> and H<sub>2</sub>O snow densities are 327.15 and 200 kg/m<sup>3</sup>, respectively.

Grain Size	CO <sub>2</sub> snow saturation thickness	H <sub>2</sub> O snow saturation thickness
50 μm	6.5 cm	5.0 cm
100 μm	10.9 cm	8.9 cm
250 μm	24.0 cm	18.8 cm
500 μm	43.1 cm	33.7 cm
1000 μm	73.8 cm	59.4 cm
1500 μm	100.2 cm	83.2 cm

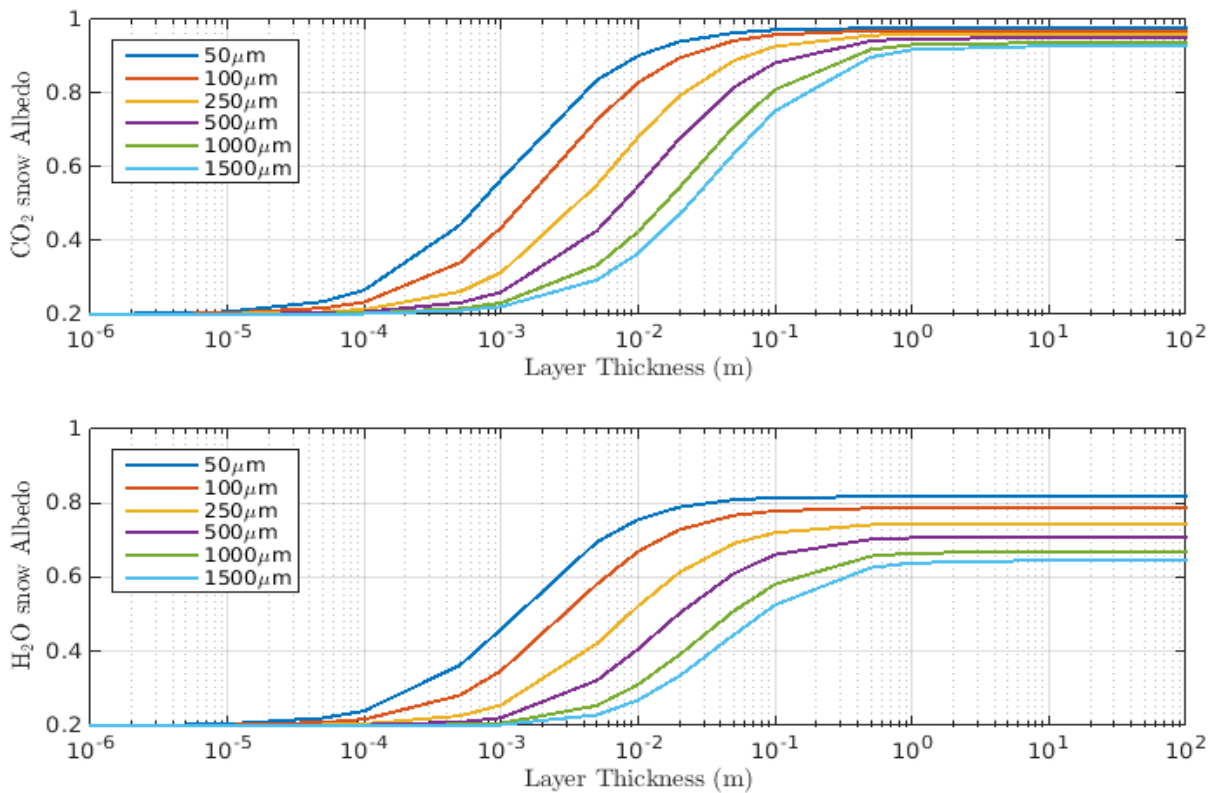


Figure 6. Broadband CO<sub>2</sub> (top) and H<sub>2</sub>O (bottom) snow albedo dependence on snow layer thickness for various effective grain sizes. The underlying surface is assumed to have a

constant albedo of 0.2. The snow density is  $327.15 \text{ kg/m}^3$  and  $200 \text{ kg/m}^3$  for  $\text{CO}_2$  and  $\text{H}_2\text{O}$  snow, respectively.

### 3.4 Dust type

The snow albedo impacts of different types of dust depend on their optical properties, and in particular on their mass absorption cross-section. Here we compare the impacts of Earth dust, Mars dust and palagonite on semi-infinite snow albedo (Fig. 7). Again, identical size distributions are assumed for each type of dust, and only the refractive indices are varied as input to Mie calculations. Mars dust has the greatest albedo impact of the three between wavelengths of 0.5 and  $2.5 \mu\text{m}$ , which contains most of the incident solar energy, while palagonite has the least. Mars dust is relatively dark due to the presence of higher amount of iron oxides [Bell III et al., 1990; Bell III, 1996; Christensen et al., 2000; Christensen et al., 2001a; Christensen et al., 2001b], combined with its large mass extinction cross-section. Although average Earth dust has a lower near-IR single-scatter albedo than the Mars dust, it also has a lower mass extinction cross-section across the spectrum, due to its larger density, leading to lower absorption per unit mass of dust, expressed via the mass absorption cross-section (Fig. 1d).

We consider “mass mixing ratio” as the mass of impurity divided by the mass of ice in which the impurity is mixed. Table 3 presents the effective  $\text{CO}_2$  snow albedo in the presence of 0.01% mass mixing ratio of dust (kg of dust / kg of ice). Dust causes a larger albedo drop in the visible region ( $\sim 0.6$ ) compared to the near-IR region ( $\sim 0.3$ ) because all three types of dust have very low single scatter albedo in the blue and green spectra while ice grains scatter very efficiently at these wavelengths (Fig. 1). Furthermore, the drop in albedo in the blue spectrum ( $\sim 0.8$ ) is much higher than the drop in the red spectrum ( $\sim 0.3$ ), helping explain the planet’s red appearance even in its cryospheric regions. Although palagonite is less absorptive than Mars dust, the spectral variations in albedo impacts of the two species are similar.

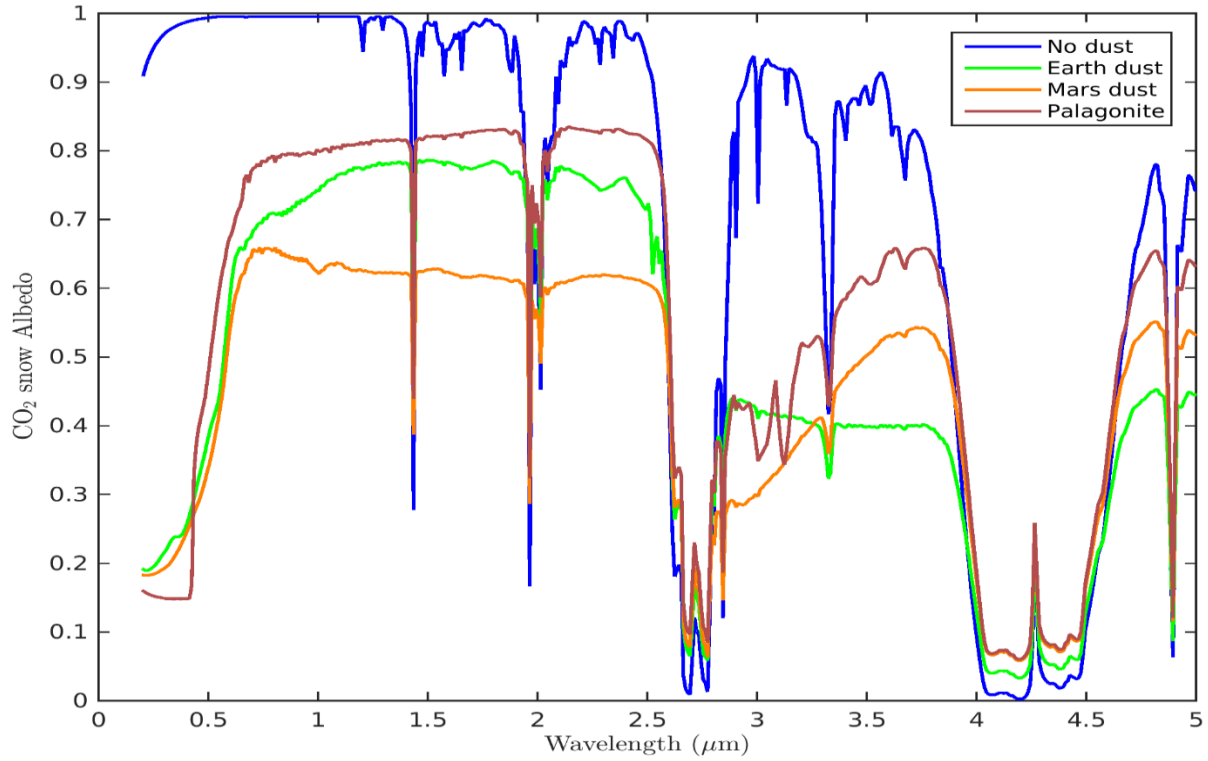


Figure 7: Impact of different types of dust on CO<sub>2</sub> snow albedo, with dust mass mixing ratio of 0.01%. The assumed snow grain size is 100  $\mu\text{m}$ .

Table 3: Impact of different types of dust on CO<sub>2</sub> broadband snow albedo (grain size of 100  $\mu\text{m}$ ), with dust mass mixing ratio of 0.01%.

	pure CO <sub>2</sub>	Earth dust	Mars Dust	Palagonite
<b>Visible (0.2-0.7 <math>\mu\text{m}</math>)</b>	0.991	0.429	0.395	0.477
<b>Near-IR (0.7-5.0 <math>\mu\text{m}</math>)</b>	0.952	0.718	0.616	0.779
<b>Broadband (0.2-5.0 <math>\mu\text{m}</math>)</b>	0.970	0.583	0.513	0.637

Table 4: Impact of different types of dust on H<sub>2</sub>O broadband snow albedo (grain size of 100  $\mu\text{m}$ ), with dust mass mixing ratio of 0.01%

	pure H <sub>2</sub> O	Earth dust	Mars Dust	Palagonite
<b>Visible (0.2-0.7 <math>\mu\text{m}</math>)</b>	0.988	0.450	0.415	0.494
<b>Near-IR (0.7-5.0 <math>\mu\text{m}</math>)</b>	0.609	0.551	0.503	0.599

<b>Broadband (0.2-5.0 <math>\mu\text{m}</math>)</b>	0.787	0.504	0.461	0.550
---	-------	-------	-------	-------

Table 4 presents the effective H<sub>2</sub>O snow albedo in the presence of 0.01% mass mixing ratio of dust. Pure H<sub>2</sub>O snow is relatively absorptive in the near-IR spectral region (Table 1, Table 4), so dust has little impact on near-IR albedo, or in the most absorptive portions of the spectrum, it even increases albedo (Fig. 8). Fundamentally, this occurs because the single-scatter albedo of dust exceeds that of H<sub>2</sub>O ice grains at wavelengths longer than about 1.5  $\mu\text{m}$ . Similar to CO<sub>2</sub> snow, the drop in albedo is large in the visible region for H<sub>2</sub>O snow. However in the near-IR region the change is less than 0.1, leading to smaller broadband albedo impacts of dust on H<sub>2</sub>O snow albedo than on CO<sub>2</sub> snow albedo. These differences indicate that dust can have greater impact on Martian cryosphere albedo than Earth cryosphere albedo due to the higher abundance of CO<sub>2</sub> ice compared to H<sub>2</sub>O ice.

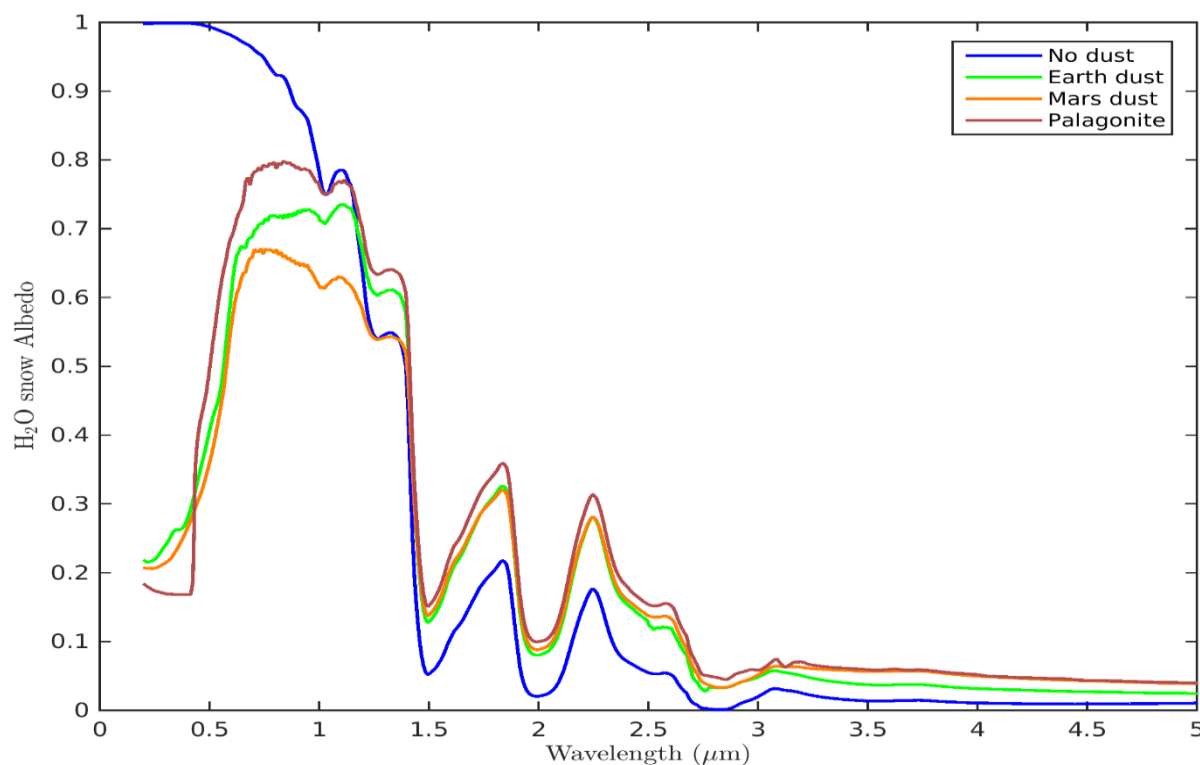


Figure 8: Impact of different types of dust on H<sub>2</sub>O snow albedo, with dust mass mixing ratio of 0.01%. The assumed snow grain size is 100  $\mu\text{m}$ .

### 3.5 Dust Concentration

Figure 9 shows the effect of varying amounts of Mars dust on CO<sub>2</sub> snow albedo (Fig. 2a). It is obvious that albedo decreases with increasing amount of dust, except in the strong absorption bands of CO<sub>2</sub> ice (e.g., near 1.4 μm, 1.9 μm, and 2.7 μm). Again we see maximum impact in the visible part of the spectrum. Saturation of the albedo from this type of dust is evident with dust mixing ratios exceeding 0.01%, with almost no difference in albedo between scenarios with 0.1% and 1% dust. Also, the strong absorption features of CO<sub>2</sub> snow at various wavelengths disappear with high dust concentrations.

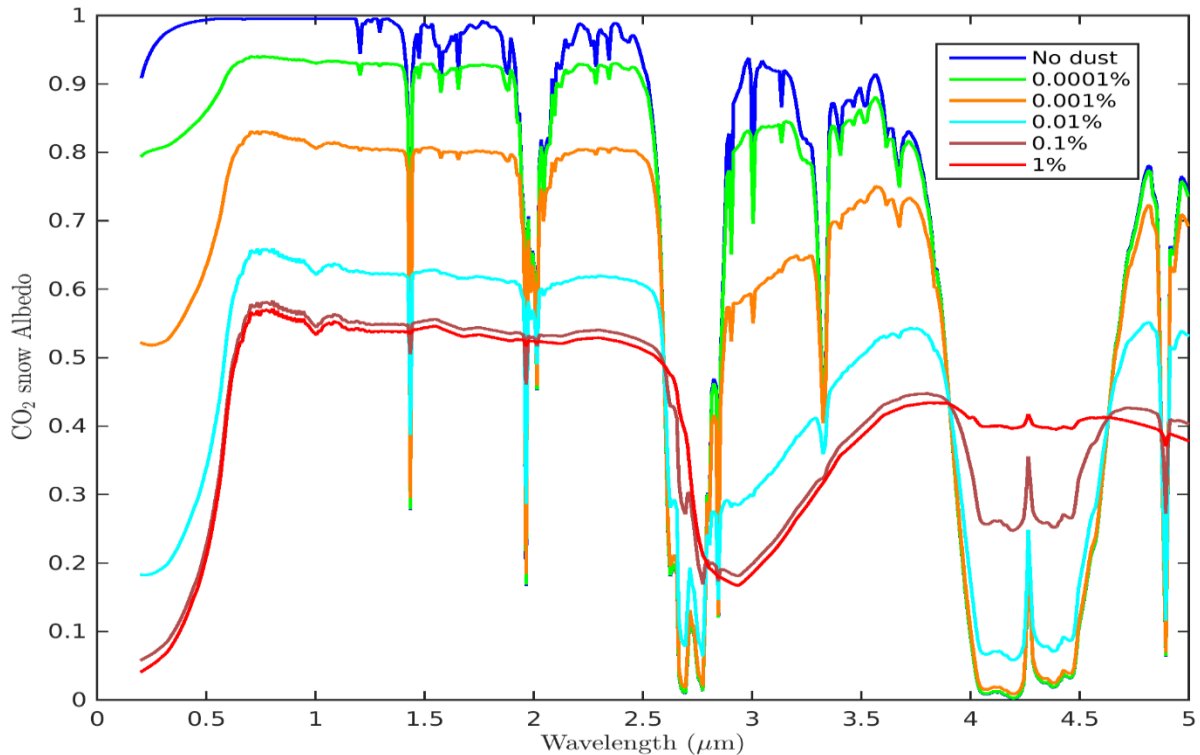


Figure 9: Impact of various amounts of Martian dust on CO<sub>2</sub> snow albedo. Snow effective grain radius is 100μm.

### 3.6 Presence of both H<sub>2</sub>O and CO<sub>2</sub> ice

#### 3.6.1 Separate layers

H<sub>2</sub>O and CO<sub>2</sub> ice interact quite differently with radiation in the visible and near-IR portions of the spectrum and also exhibit different sensitivities to different physical parameters. These ice types are also known to co-exist on the surface of Mars [e.g. *Byrne et al., 2008; Brown et*



al., 2014]. Here, we explore the albedo effects associated with thin slabs of one type of ice overlying the other, building on sensitivity studies conducted by *Warren et al.*, [1990]. Figure 10 shows spectral albedo of surfaces with H<sub>2</sub>O snow on top of CO<sub>2</sub> snow (scenario shown in figure 2c), and figure 11 shows albedo with the reverse situation (scenario shown in figure 2b).

Albedo decreases markedly with the presence of thin slabs of H<sub>2</sub>O snow on top of CO<sub>2</sub> snow. This decrease occurs more rapidly with increasing thickness of H<sub>2</sub>O ice than the rate of albedo increase that occurs with increasing thickness of CO<sub>2</sub> snow overlying H<sub>2</sub>O snow. For a grain size of 100 μm, about 2.5 cm of H<sub>2</sub>O snow is required to completely mask out the albedo effect of CO<sub>2</sub> snow (Table 5), whereas about 5.5 cm of CO<sub>2</sub> snow is required to completely mask out the albedo effect of underlying H<sub>2</sub>O snow (Table 6). Again, differences are more pronounced in the near-IR spectrum (e.g., Fig. 3, Table 1), where the contrast in absorptivity between CO<sub>2</sub> and H<sub>2</sub>O ice is greater (Tables 5 and 6). Rows marked with an asterisk (\*) correspond to saturation thickness. In summary, very little H<sub>2</sub>O snow is needed to mask the presence of underlying CO<sub>2</sub> snow, whereas a larger thickness of CO<sub>2</sub> snow is needed to prevent underlying, more absorptive H<sub>2</sub>O snow from effecting surface albedo.

*Warren et al.*, [1990] determined that the presence of H<sub>2</sub>O snow on top of CO<sub>2</sub> snow will increase the net surface albedo, contrary to the analysis presented here. The CO<sub>2</sub> ice refractive indices applied in that study, however, were measured using unpurified commercial dry ice [*Egan and Spagnolo*, 1969], and data in the 1.0-2.5 μm spectral region were extrapolated from the 0.3-1.0 μm spectral region. The higher quality measurements on pure CO<sub>2</sub> ice provided by *Hansen* [1997, 2005], and applied here, indicate that CO<sub>2</sub> ice is much less absorptive than previously assumed, leading to our opposite conclusion.

Author Manuscript

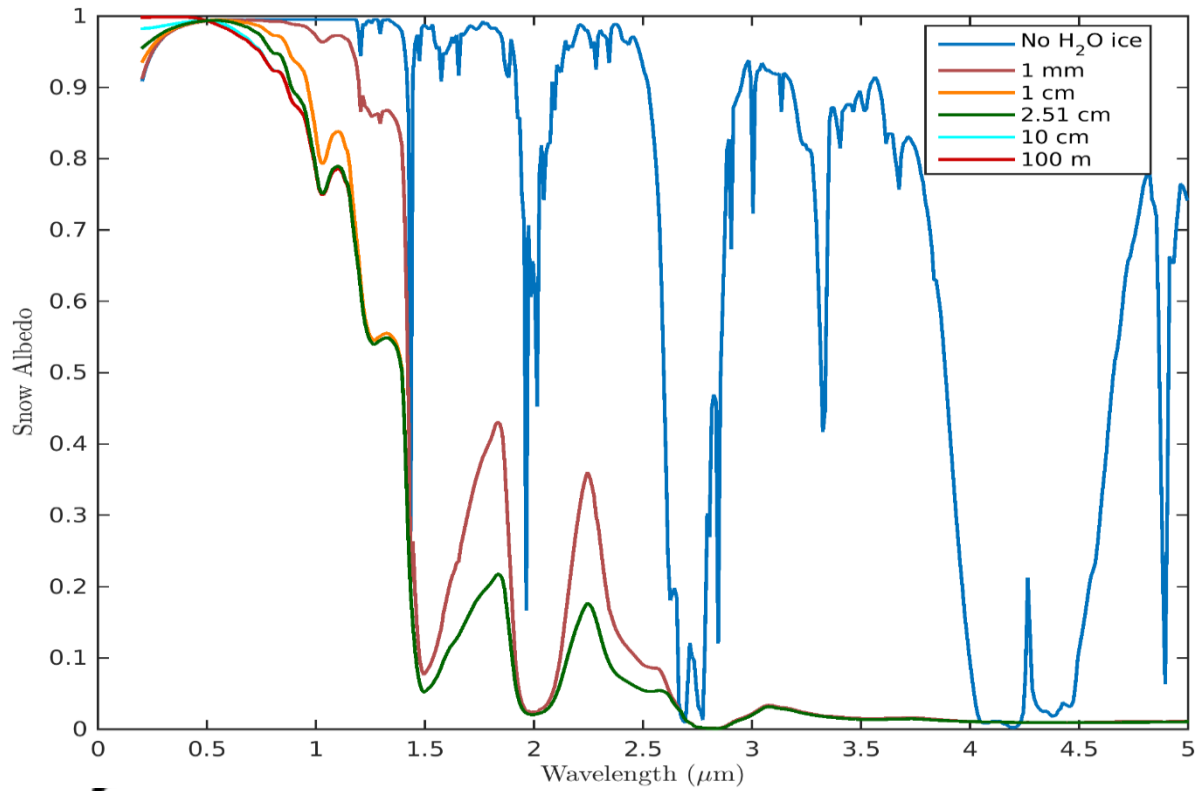


Figure 10: Spectral albedo of surfaces with H<sub>2</sub>O snow layers of varying thickness on top of CO<sub>2</sub> snow. The green curve thickness corresponds to saturation thickness.

Author Mar

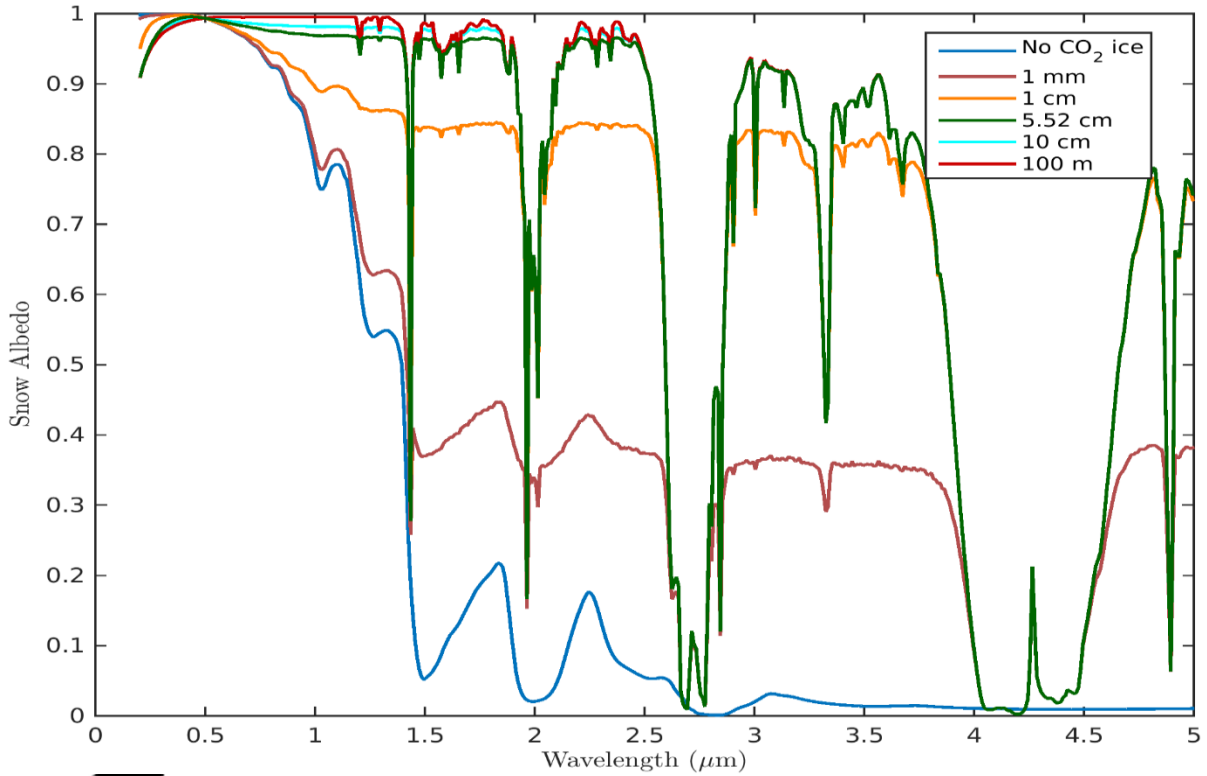


Figure 11: Spectral albedo of surfaces with CO<sub>2</sub> snow layers of varying thickness on top of H<sub>2</sub>O snow. The green curve thickness corresponds to saturation thickness.

Table 5: Broadband albedos of surfaces with H<sub>2</sub>O snow layers on top of CO<sub>2</sub> snow

H <sub>2</sub> O layer thickness	Vis	Near-IR	Broadband
0	0.991	0.952	0.970
1 mm	0.991	0.739	0.857
1 cm	0.991	0.639	0.804
2.51 cm*	0.987	0.618	0.793
10 cm	0.990	0.610	0.787
100 m	0.988	0.609	0.787

\*Saturation thickness (section 3.3)

Table 4: Broadband albedos of surfaces with CO<sub>2</sub> snow layers on top of H<sub>2</sub>O snow

CO <sub>2</sub> layer thickness	Vis	Near-IR	Broadband
0	0.988	0.609	0.787
1 mm	0.988	0.703	0.837
1 cm	0.989	0.869	0.925
5.52 cm*	0.989	0.934	0.960

10 cm	0.990	0.943	0.965
100 m	0.991	0.952	0.970

\*Saturation thickness (section 3.3)

Figure 12 shows the broadband net surface albedo dependence on layer thickness for different snow types. The black lines indicate the saturation thickness (section 3.3) for the two scenarios discussed above. To further explore the behavior of albedo with layer thickness, we divide each curve into two regions: with thickness lesser and higher than saturation thickness. Table 7 lists the slopes of albedo per layer thickness for these two regions. For top layer thickness less than saturation thickness (first region), higher slope (in absolute values) of data shown in Fig. 12a than 12b substantiates the conclusion that H<sub>2</sub>O snow is harder to mask out compared to CO<sub>2</sub> snow. However, for the second region with thickness higher than saturation thickness, the scenario with overlying CO<sub>2</sub> snow (Fig 12b) demonstrates higher absolute slope than the reverse situation. This indicates that H<sub>2</sub>O snow is less sensitive to thickness variation (once a minimum threshold is reached), owing to its more absorptive nature in the near-IR spectrum compared to CO<sub>2</sub> snow.

Author Manuscript

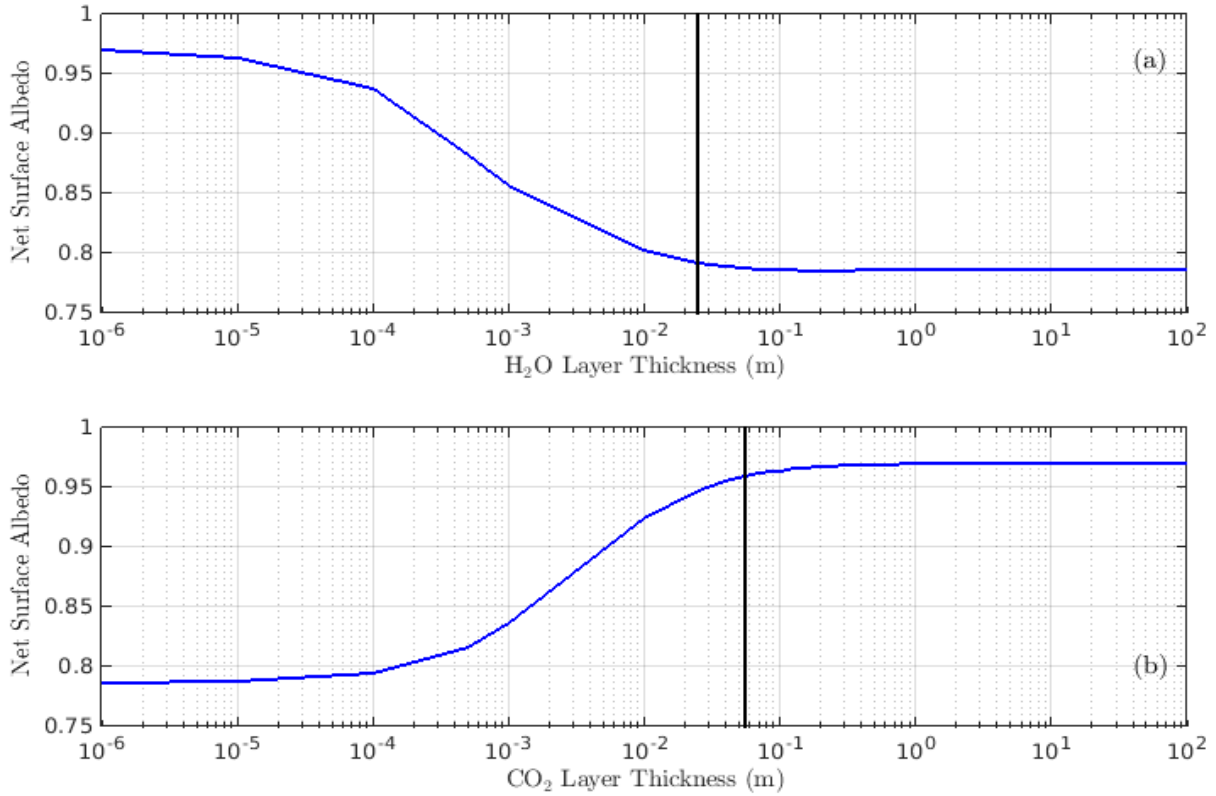


Figure 12: Dependence of net surface broadband snow albedo on layer thickness for (a) an H<sub>2</sub>O snow layer on top of a semi-infinite CO<sub>2</sub> snow layer, and (b) a CO<sub>2</sub> snow layer on top of a semi-infinite H<sub>2</sub>O snow layer. The black line indicates the saturation thickness for each case. Snow grain size is assumed to be 100 μm in both cases.

Table 1: Slopes of albedo per change in layer thickness for the two scenarios shown in figure 12

Thickness regime	H <sub>2</sub> O snow layer on top of CO <sub>2</sub> snow layer (Fig 11a)	CO <sub>2</sub> snow layer on top of H <sub>2</sub> O snow layer (Fig 11b)
<b>Less than saturation thickness</b>	-7.10 m <sup>-1</sup>	+3.14 m <sup>-1</sup>
<b>Higher than saturation thickness</b>	-5.54×10 <sup>-5</sup> m <sup>-1</sup>	+1.05×10 <sup>-4</sup> m <sup>-1</sup>

### 3.6.2 Mixed layers

In addition to the possibility of different snow types being present as separate layers, both types of snow can also become mixed together on the surface of Mars [e.g. *Brown et al.*,

2014]. In this section, we explore the net surface albedo changes caused by one snow type becoming mixed with the other snow type. In practice, this is simulated by treating the less abundant ice type as an externally-mixed “impurity” with specified mass mixing ratio (scenario shown in figure 2d), analogous to the treatment of dust described earlier. Figure 13 shows the net surface albedo when H<sub>2</sub>O snow is present as an impurity within CO<sub>2</sub> snow, and figure 14 shows the net surface albedo for the reverse situation. We assume a semi-infinite snow layer, and effective grain size of 100 μm for both snowpacks.

Broadband (near-IR) albedo drops by ~0.18 (~0.34) for an associated increase of H<sub>2</sub>O snow from 0% to 10% within CO<sub>2</sub> snow. However, broadband (near-IR) albedo increases by ~0.10 (~0.18) in the reverse situation. This is consistent with our earlier findings that H<sub>2</sub>O snow is relatively darker (especially in the near-IR region) compared to CO<sub>2</sub> snow, hence causing larger impact on net surface albedo. 0.01% of H<sub>2</sub>O snow is sufficient to reduce the net broadband albedo of the mixture by 0.03, while 1% of CO<sub>2</sub> snow is required to increase the net surface broadband albedo of the mixture by same amount.

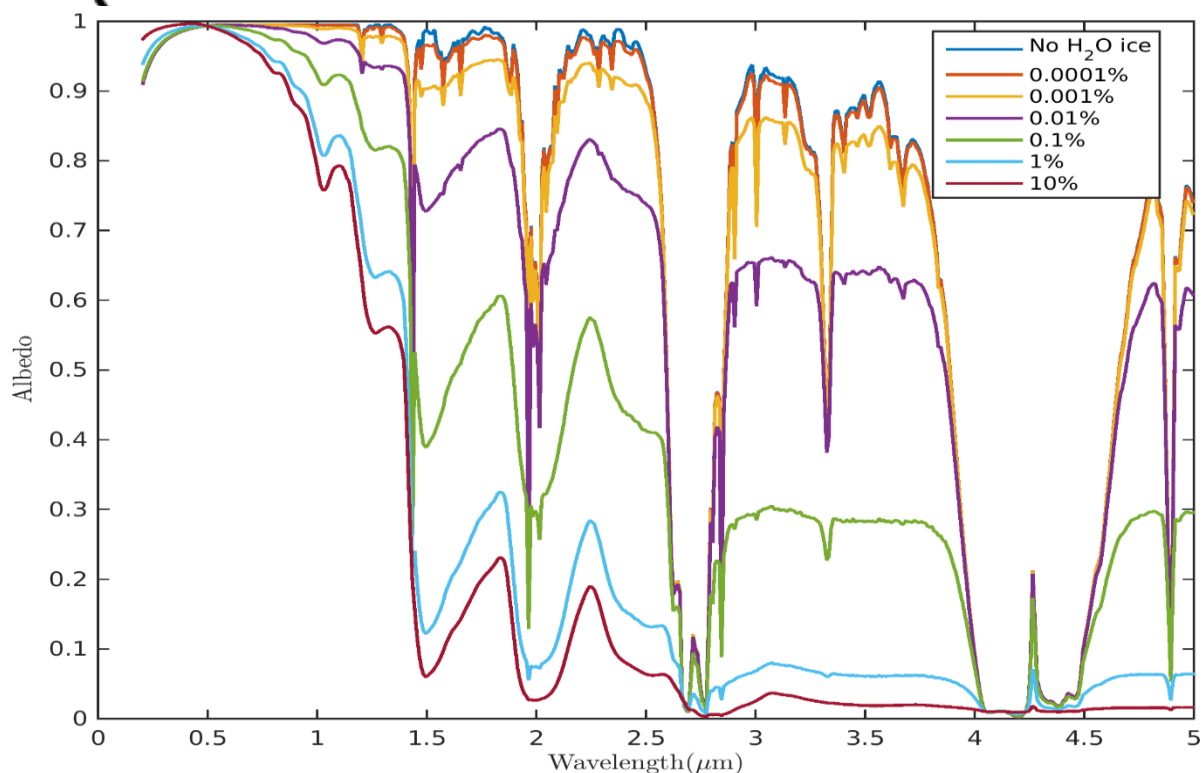


Figure 13: Spectral albedo of surfaces with H<sub>2</sub>O ice present as an impurity within CO<sub>2</sub> snow. Effective grain size for both snow types is 100 μm and the layer is semi-infinite.

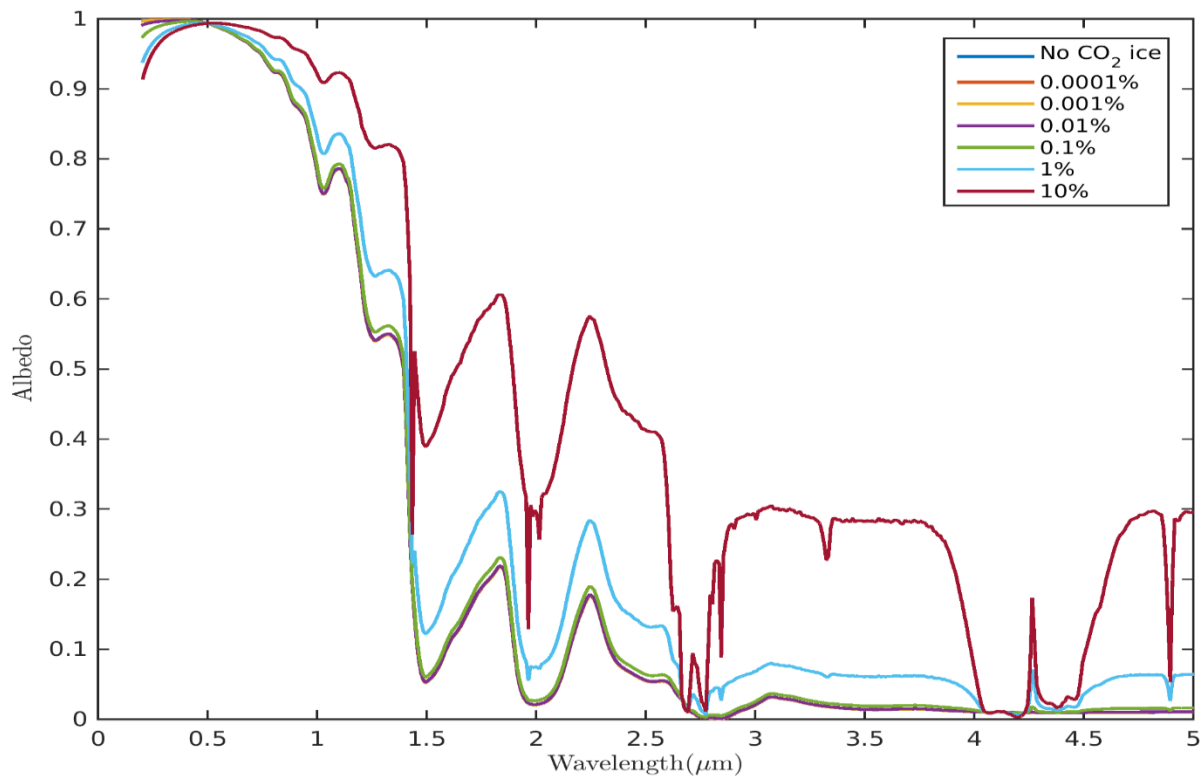


Figure 14: Spectral albedo of surfaces with CO<sub>2</sub> ice present as an impurity within H<sub>2</sub>O snow. Effective grain size for both snow types is 100 μm and the layer is semi-infinite.

#### 4 Comparison with observed Martian albedo

In this section, we compare our simulations with some observations of surface reflectance in the Martian cryosphere and try to identify parameter combinations that produce reasonable agreement between the modeled and observed data. We first note that SNICAR produces directional-hemispherical albedo, whereas the CRISM and OMEGA observations evaluated here are bidirectional reflectances. This discrepancy renders the model-observation comparison imperfect, but the analysis does have some usefulness in illustrating broad agreement between modeled and observed spectral reflectance features, and in identifying general ranges of physical parameters that produce reasonable modeled spectra in different environments.

#### 4.1 Comparison with CRISM measurements

We obtained spectral reflectance data for one location in the Southern Hemisphere [point A, Fig. 3 of *Brown et al., 2014*] identified to have a majority of CO<sub>2</sub> ice (hereafter location S), and one location from the Northern Hemisphere [point B, Fig 4c of *Brown et al., 2012*] identified to have mostly H<sub>2</sub>O ice (hereafter location N). The observed reflectance were obtained using radiance measurements from CRISM in the 1-4  $\mu\text{m}$  spectral range. Therefore we only compare our simulations in this spectral range.

Since the reflectance data display a time dependency, we choose two of the least noisy end-member (i.e., most different) observed spectra for each location. Then we determine the best fit for each location by minimizing the weighted RMSE between each of the identified spectral reflectance curves and our hemispheric albedo simulations, which span a wide range of the parameter space described earlier. Spectral weighting for the RMSE calculation is done with the same solar spectral irradiance measurements [*Labs and Neckel, 1968*] applied throughout this study. Therefore, reflectance values for longer wavelengths are weighted less strongly and consequently do not fit as well with observations. We also note that reflectance measurements at wavelengths longer than 2.5  $\mu\text{m}$  are not very reliable (on Earth too) because there is very little incoming solar energy at these wavelengths.

Table 8. Best fit parameter combinations for each Mars location. The H<sub>2</sub>O ice at Location S is simulated as a mixture within the CO<sub>2</sub> snow, as opposed to a distinct layer.

	Location S		Location N		
	Ls=276	Ls=337		Ls=13	Ls=65
CO <sub>2</sub> ice grain size	1000 $\mu\text{m}$	3000 $\mu\text{m}$	H <sub>2</sub> O ice grain size	100 $\mu\text{m}$	500 $\mu\text{m}$
H <sub>2</sub> O ice grain size	100 $\mu\text{m}$	200 $\mu\text{m}$	CO <sub>2</sub> ice grain size	n/a	n/a
Amount of H <sub>2</sub> O ice	0.024%	0.07%	Amount of CO <sub>2</sub> ice	n/a	n/a
Amount of dust	0.0042%	0.003%	Amount of dust	0.06%	0.01%
RMSE (solar weighted)	0.06	0.07	RMSE	0.055	0.057

Table 8 lists the best fit values of various parameters along with spectrally-weighted RMSE values for both locations. The presence of any CO<sub>2</sub> ice tends to increase the RMSE at location N. This happens because observations from location N occurred during early spring



to mid-summer in that hemisphere, when there is likely no CO<sub>2</sub> ice present on the surface [e.g. *Brown et al.*, 2014]. Location S needs about an order of magnitude less dust amount as compared to location N for optimal fitting. One reason for this is that Location S is deemed to have some coincident H<sub>2</sub>O ice, which functions as a competing impurity to dust because H<sub>2</sub>O snow substantially darkens albedo in the near-IR spectral region. For location S, changing CO<sub>2</sub> ice grain size does not have any significant impact on RMSE, while the H<sub>2</sub>O ice grain size has significant impact on RMSE for location N. This is consistent with our results described in section 3.2.

Figures 15 and 16 show the observed spectral reflectance curves along with simulated albedo using parameter values shown in Table 8. We observe an outlier point at 2.7 μm wavelength in the observed data for both locations and at all times. Reflectance values at this wavelength are uncharacteristically higher than at nearby wavelengths, whereas both CO<sub>2</sub> and H<sub>2</sub>O snows have very high absorptivity at this wavelength (Fig. 3). This leads us to suggest that the high observed reflectance at this wavelength are spurious, and may be due either to an artefact of the measuring spectrometer (CRISM), atmospheric anomalies associated with dust or clouds [*Brown et al.*, 2010], and/or a calibration issue in the retrieval of surface reflectance at that wavelength. We also emphasize again that the low intensity of sunlight at this wavelength renders the reflectance measurements less certain than at shorter wavelengths.

Author Manuscript

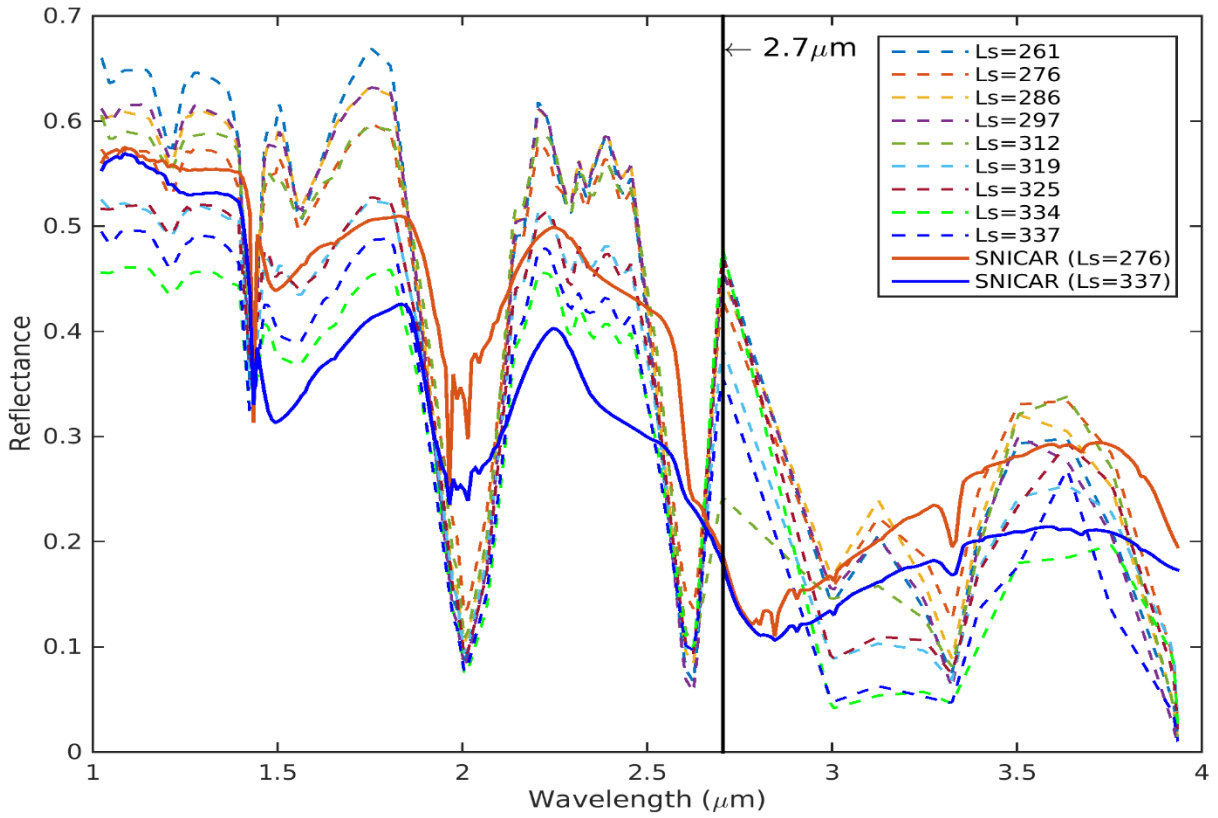


Figure 15: Observed reflectance for location S (dotted curves) along with modeled albedo using best-fit parameters (solid blue curve). The black vertical line at 2.7 μm indicates the outline described in the text.

Author Ma

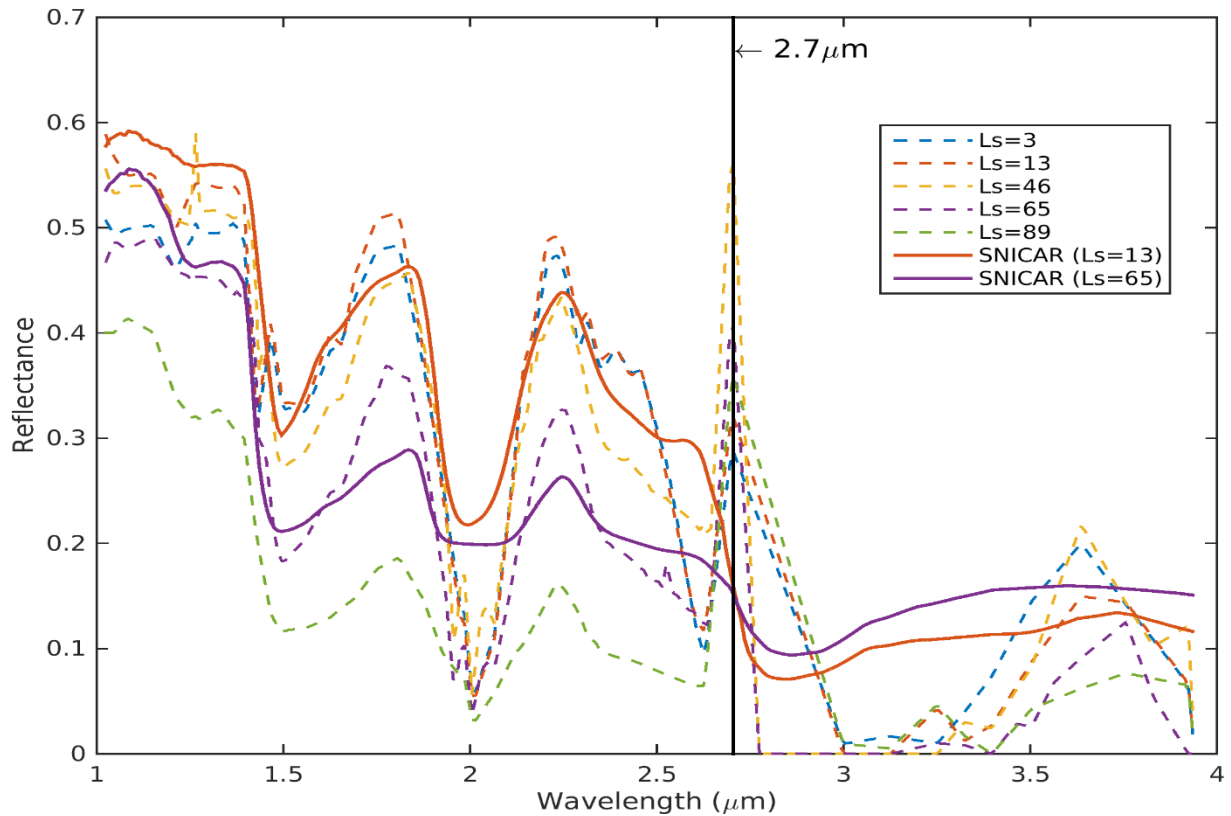


Figure 16: Same as fig. 15 but for location N

## 4.2 Comparison with OMEGA measurements

We also obtained spectral reflectance for Observation 2621\_1 from the OMEGA instrument [see Fig. 18 from *Appéré et al.*, 2011; shown later here], and modeled spectral reflectance of snow mixture simulated with a different radiative transfer model developed by *Douté and Schmitt* [1988].

As shown in Table 9 and Fig. 17, *Appéré et al.*, [2011] achieved good agreement between simulated near-IR snow reflectance and OMEGA observations of a CO<sub>2</sub>-rich deposit by assuming a mixed CO<sub>2</sub>/H<sub>2</sub>O snow configuration with a CO<sub>2</sub> grain size of 7 μm, which interestingly is much larger than what is deemed to be realistic under most conditions [*Barr and Milkovich*, 2008]. We also achieved a reasonable fit (spectrally-weighted RMSE of 0.02) against the OMEGA observations presented by *Appéré et al.*, [2011] with a mixed CO<sub>2</sub> and H<sub>2</sub>O configuration of SNICAR applying a smaller CO<sub>2</sub> grain radius and slightly

different mass fractions of dust and H<sub>2</sub>O (Table 9; Fig. 17), though admittedly the fit is not quite as good as that obtained by *Appéré et al.* [2011]. It is plausible that the better agreement obtained by *Appéré et al.* [2011] is due to their use of a directional reflectance radiative transfer model [*Douté and Schmitt, 1988*], which provides a more consistent comparison with the measurements. Uncertainties in the observations, however, are described by *Appéré et al.* [2011] to be roughly 20%, indicating that both sets of modeled spectra are within the range of uncertainty. Finally, we note that the quality of our fit ceases to change much with larger grain sizes of CO<sub>2</sub> ice.

Table 9: Comparison of best-fit parameters between SNICAR and *Appéré et al.*, [2011]

	SNICAR	<i>Appéré et al.</i> , [2011]
CO <sub>2</sub> ice grain size	3000 μm	7 cm
Amount of CO <sub>2</sub> ice	99.83%	99.75%
H <sub>2</sub> O ice grain size	100 μm	200 μm
Amount of H <sub>2</sub> O ice	0.16%	0.19%
Dust grain size	1.5 μm	13 μm
Amount of dust	0.0094%	0.06%
RMS <sub>fit</sub> (solar weighted)	0.027	0.016

Author Manuscript

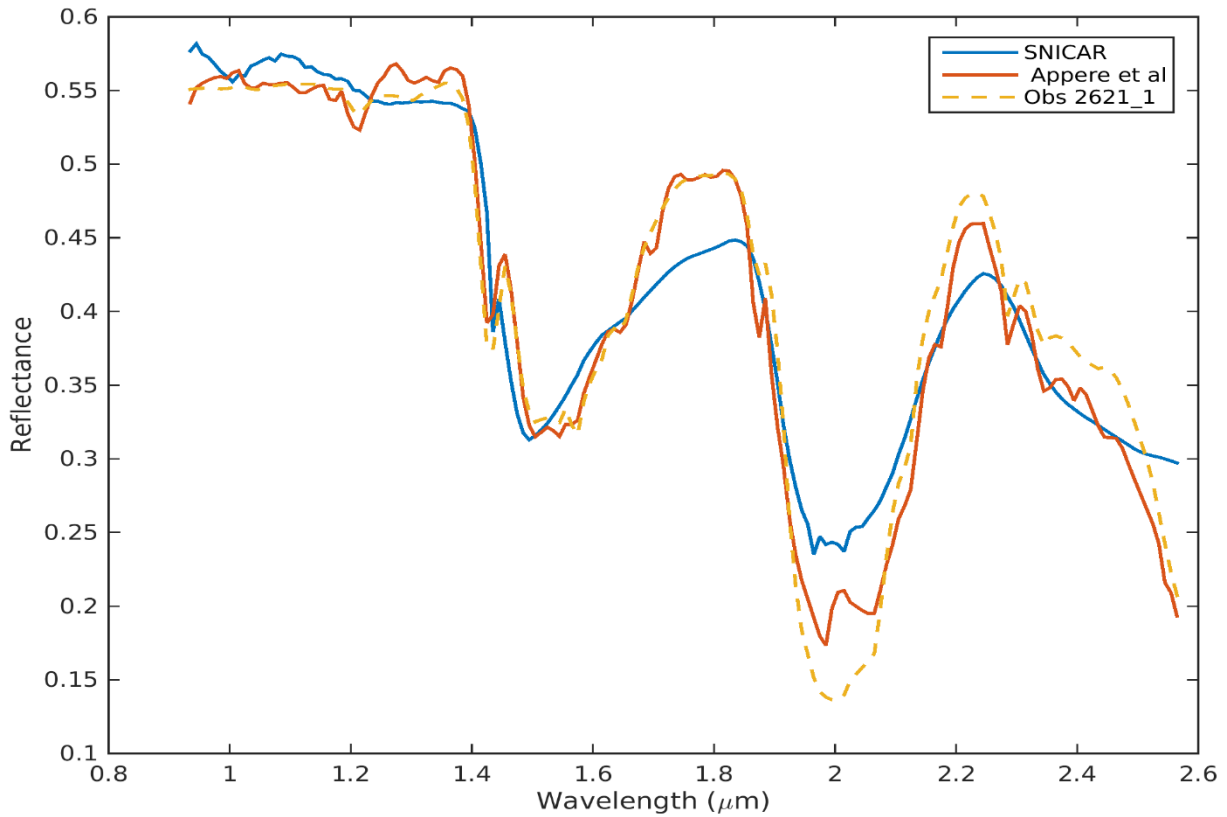


Figure 17: Comparison of best fit albedo using SNICAR and the model applied by *Appéré et al.*, [2011] against data from OMEGA observation 2621\_1.

## 5 Conclusions

We have simulated the spectral albedo of CO<sub>2</sub> snow using an enhanced 480-band version of SNICAR, which was previously developed for terrestrial snow. We explored CO<sub>2</sub> snow albedo across the entire solar spectrum, including UV, visible and near-IR wavelengths. Our analysis shows significant differences between H<sub>2</sub>O and CO<sub>2</sub> snow albedos. H<sub>2</sub>O snow is about 2 times more absorptive than CO<sub>2</sub> snow in the near-IR region, and 7 times more absorptive averaged over the entire solar spectrum. CO<sub>2</sub> snow albedo shows very little dependence on solar zenith angle and a weaker dependence on grain size than H<sub>2</sub>O snow. The broadband albedo of CO<sub>2</sub> snow decreases by only 0.064 as effective grain size increases from 50 to 1500 μm.

The presence of thin snow layers exposes underlying surfaces to incoming radiation, hence impacting the surface albedo. The saturation thicknesses for CO<sub>2</sub> snow and H<sub>2</sub>O snow range from approximately 6.5 – 100 cm and 5 – 83 cm, respectively, for effective grain sizes ranging from 50 to 1500 μm, though we caution again that these thicknesses may be smaller with non-spherical ice particles. Non-spherical grains scatter less strongly in the forward direction, thereby decreasing the penetration depth of solar radiation. Thicker CO<sub>2</sub> snow is required to negate the impact of underlying surface because CO<sub>2</sub> ice grains scatter more strongly than H<sub>2</sub>O ice grains, especially in the near-IR spectrum. The presence of 0.01% dust reduces the broadband albedo of CO<sub>2</sub> snow by about 50%, with Martian dust being the darkest type of dust explored here, followed by typical Earth dust and palagonite. The spectral shape of albedo changes caused by palagonite, which is often used as a Martian dust analog, closely follow those of Mars dust, but palagonite is not as absorptive as Mars dust. The impact of dust on CO<sub>2</sub> snow albedo saturates after its mass mixing ratio exceeds roughly 0.1%.

Because of the contrasting properties of H<sub>2</sub>O and CO<sub>2</sub> ice in the near-IR spectrum, different layering and mixing configurations of these types of snow can have substantial impact on net surface albedo. With an effective grain size of 100 μm, only about 2.5 cm of H<sub>2</sub>O snow is needed to mask the influence of underlying CO<sub>2</sub> snow on net surface albedo (Table 5), while more than double this amount of CO<sub>2</sub> snow is needed to mask the influence of H<sub>2</sub>O snow (Table 6). Such effects are relevant for the perennial H<sub>2</sub>O ice caps of Mars, and where water vapor from the atmosphere condenses on top of CO<sub>2</sub> ice in other areas of the planet. When both snow types are present as a mixture rather than separate layers, 0.01% of H<sub>2</sub>O snow reduces the broadband albedo of CO<sub>2</sub> snow by 0.03, while 1% of CO<sub>2</sub> snow is required to increase the broadband albedo of H<sub>2</sub>O snow by the same amount.

With the identification of optimal snow parameter combinations, our results show a decent agreement between modeled spectral albedo and observed reflectance of the Martian polar ice caps in the 1–4 μm spectral range. The CRISM data exhibit anomalously high reflectance at 2.7 μm, which cannot be explained with presence of either CO<sub>2</sub> or H<sub>2</sub>O ice, as both media are highly absorptive at this wavelength. SNICAR also provides realistic best-fit parameters for

matching OMEGA near-IR observations, though the spectral fit is not as good as that achieved previously with a directional reflectance model [Appéré *et al.*, 2011]. Simulations presented here could potentially be used in combination with observed data to refine the calibration of surface albedo retrieval algorithms. Model results can also be used to interpolate measurements to higher spectral resolution. The new spectrally resolved albedos for CO<sub>2</sub> snow presented here have potentially wide applicability to any planet or system with CO<sub>2</sub> ice, especially Mars.

### Acknowledgements

We are grateful to Michael Mischna, Mike Wolff, Jeffrey Johnson, Adrian Brown, and Thomas Appéré for providing, respectively, CO<sub>2</sub> ice refractive indices derived from Gary Hansen's measurements, Martian dust optical properties, palagonite optical properties, surface reflectivity derived from CRISM observations, and observed and modeled albedo derived from OMEGA observations. A single-layer implementation of SNICAR can be operated interactively on the web at: <http://snow.engin.umich.edu>. This work was partially supported by NASA NNX13AN29G and NSF ARC-1253154.

### References

- Appéré, T., B. Schmitt, Y. Langevin, S. Douté, A. Pommerol, F. Forget, A. Spiga, B. Gondet, and J. F. Blaring (2011), Winter and spring evolution of northern seasonal deposits on Mars from OMEGA on Mars Express, *J. Geophys. Res.*, 116, E05001, doi:10.1029/2010JE003762.
- Balkanski, Y., M. Schulz, T. Claquin, and S. Guibert (2007), Reevaluation of Mineral aerosol radiative forcings suggests a better agreement with satellite and AERONET data. *Atmospheric Chemistry and Physics*, 7(1), 81-95.
- Banin, A., T. X. Han, I. Kan, and A. Cicelsky (1997), Acidic volatiles and the Mars soil, *J. Geophys. Res.*, 102(E6), 13341–13356, doi:10.1029/97JE01160.
- Barr, A. G., and S. M. Milkovich, (2008), Ice grain size and the rheology of the martian polar deposits. *Icarus*, 194(2), 513-518, doi:10.1016/j.icarus.2007.11.018.

- Bell III, J. F., T. B. McCord, and P. D. Owensby (1990), Observational evidence of crystalline iron oxides on Mars. *J. Geophys. Res.*, 95(B9), 14447–14461, doi:10.1029/JB095iB09p14447.
- Bell III, J. F. (1996). Iron, sulfate, carbonate, and hydrated minerals on Mars, in " Mineral Spectroscopy: A Tribute to Roger G. Burns," *Geochemical Society Special Publication 5* (MD Dyar, C. McCammon, and MW Schaefer, eds.), 359-380.
- Bibring, J. P., Y. Langevin, A. Gendrin, B. Gondet, F. Poulet, M. Berthé, A. Soufflot, R. Arvidson, N. Mangold, J. Mustard, and P. Drossart (2005), Mars surface diversity as revealed by the OMEGA/Mars Express observations. *Science*, 307(5715), 1576-1581.
- Bibring, J. P., Y. Langevin, F. Poulet, A. Gendrin, B. Gondet, M. Berthé, A. Soufflot, P. Drossart, M. Combes, G. Bellucci, and V. Moroz (2004). Perennial water ice identified in the south polar cap of Mars. *Nature*, 428(6983), 627-630.
- Bonev, B. P., G. B. Hansen, D. A. Glenar, P. B. James, and J. E. Bjorkman (2008). Albedo models for the residual south polar cap on Mars: Implications for the stability of the cap under near-perihelion global dust storm conditions. *Planetary and Space Science*, 56(2), 181-193, doi:10.1016/j.pss.2007.08.003
- Brown, A. J., W. M. Calvin, P. C. McGuire, and S. L. Murchie (2010), Compact Reconnaissance Imaging Spectrometer for Mars (CRISM) south polar mapping: First Mars year of observations, *J. Geophys. Res.*, 115, E00D13, doi:10.1029/2009JE003333.
- Brown, A. J., W. M. Calvin, and S. L. Murchie (2012), Compact Reconnaissance Imaging Spectrometer for Mars (CRISM) north polar springtime recession mapping: First 3 Mars years of observations, *J. Geophys. Res.*, 117, E00J20, doi:10.1029/2012JE004113.
- Brown, A. J., S. Piqueux, and T. N. Titus, (2014), Interannual observations and quantification of summertime H<sub>2</sub>O ice deposition on the Martian CO<sub>2</sub> ice south polar cap. *Earth and Planetary Science Letters*, 406, 102-109.



Byrne, S., M. T. Zuber, and G. A. Neumann (2008), Interannual and seasonal behavior of Martian residual ice-cap albedo. *Planetary and Space Science*, 56(2), 194-211.

Christensen, P. R., J. L. Bandfield, R. N. Clark, K. S. Edgett, V. E. Hamilton, T. Hoefen, H. H. Kieffer, R. O. Kuzmin, M. D. Lane, M. C. Malin, R. V. Morris, J. C. Pearl, R. Pearson, T. L. Roush, S. W. Ruff and M. D. Smith (2000), Detection of crystalline hematite mineralization on Mars by the Thermal Emission Spectrometer: Evidence for near-surface water, *J. Geophys. Res.*, 105(E4), 9623–9642, doi:10.1029/1999JE001093.

Christensen, P. R., J. L. Bandfield, V. E. Hamilton, S. W. Ruff, H. H. Kieffer, T. N. Titus, M. C. Malin, R. V. Morris, M. D. Lane, R. L. Clark, B. M. Jakosky, M. T. Mellon, J. C. Pearl, B. J. Conrath, M. D. Smith, R. T. Clancy, R. O. Kuzmin, T. Roush, G. L. Mehall, N. Gorelick, K. Bender, K. Murray, S. Dason, E. Greene, S. Silverman, M. Greenfield (2001a), Mars Global Surveyor Thermal Emission Spectrometer experiment- Investigation description and surface science results. *J. Geophys. Res.*, 106(E10), 23823–23871, doi:10.1029/2000JE001370.

Christensen, P. R., R. V. Morris, M. D. Lane, J. L. Bandfield, and M. C. Malin (2001b), Global mapping of Martian hematite mineral deposits: Remnants of water-driven processes on early Mars, *J. Geophys. Res.*, 106(E10), 23873–23885, doi:10.1029/2000JE001415.

Clancy, R. T., S. W. Lee, G. R. Gladstone, W. W. McMillan, and T. Roush (1995), A new model for Mars atmospheric dust based upon analysis of ultraviolet through infrared observations from Mariner 9, Viking, and Phobos, *J. Geophys. Res.*, 100, 5251– 5264.

Clark, R. N., T. V. King, M. Klejwa, G. A. Swayze, and N. Vergo (1990), High spectral resolution reflectance spectroscopy of minerals. *J. Geophys. Res.*, 95(B8), 12653–12680, doi:10.1029/JB095iB08p12653.

Douté, S., and B. Schmitt (1998), A multilayer bidirectional reflectance model for the analysis of planetary surface hyperspectral images at visible and near-infrared wavelengths, *J. Geophys. Res.*, 103(E13), 31367–31389, doi:10.1029/98JE01894.

European Committee for Standardization. 2003. EN 1991-1- 1: Eurocode 1 – Actions on Structures – Part 1–3: General Actions – Snow Loads. European Committee for Standardization: Brussels

Flanner, M. G., C. S. Zender, J. T. Randerson, and P. J. Rasch (2007), Present day climate forcing and response from black carbon in snow, *J. Geophys. Res.*, 112, D11202, doi:10.1029/2006JD008003.

Flanner, M. G., C. S. Zender, P. G. Hess, N. M. Mahowald, T. H. Painter, V. Ramanathan, and P. J. Rasch (2009), Springtime warming and reduced snow cover from carbonaceous particles, *Atmos. Chem. Phys.*, 9, 2481-2497.

Forget, F. (1998), Mars CO<sub>2</sub> ice polar caps. In *Solar System Ices*, Springer Netherlands, 477-507.

Forget, F., F. Hourdin, and O. Talagrand (1998), CO<sub>2</sub> snowfall on Mars: Simulation with a general circulation model. *Icarus*, 131(2), 302-316.

Fu, Q. (2007), A new parameterization of an asymmetry factor of cirrus clouds for climate models. *J. Climate*, 64, 4140-4150, doi: 10.1175/2007JAS2289.1

Hansen, G. B. (1997), The infrared absorption spectrum of carbon dioxide ice from 1.8 to 333  $\mu\text{m}$ , *J. Geophys. Res.*, 102(E9), 21569–21587, doi:10.1029/97JE01875.

Hansen, G. B. (1999), Control of the radiative behavior of the Martian polar caps by surface CO<sub>2</sub> ice: Evidence from Mars Global Surveyor measurements, *J. Geophys. Res.*, 104(E7), 16471–16486, doi:10.1029/1998JE000626.

Hansen, G. B. (2005), Ultraviolet to near-infrared absorption spectrum of carbon dioxide ice from 0.174 to 1.8  $\mu\text{m}$ . *J. Geophys. Res.*, 110, E11003, doi:10.1029/2005JE002531.

Hansen, J. E., and L. D. Travis (1974), Light scattering in planetary atmospheres. *Space Science Reviews*, 16(4), 527-610.

Herr, K. C., and G. C. Pimentel (1969), Infrared absorptions near three microns recorded over the polar cap of Mars. *Science*, 166(3904), 496-499.

Kieffer, H. H., and T. N. Titus, (2001), TES mapping of Mars' north seasonal cap. *Icarus*, 154(1), 162-180.

Kieffer, H. H., T. N. Titus, K. F. Mullins, and P. R. Christensen (2000), Mars south polar spring and summer behavior observed by TES: Seasonal cap evolution controlled by frost grain size. *J. Geophys. Res.*, 105(E4), 9653–9699, doi:10.1029/1999JE001136.

Labs, D., H. Neckel (1968), The Radiation of the Solar Photosphere from 2000 Å to 100 μm. *Zeitschrift für Astrophysik*, 69, 1.

Langevin, Y., J.-P. Bibring, F. Montmessin, F. Forget, M. Vincendon, S. Douté, F. Poulet, and B. Gondet (2007), Observations of the south seasonal cap of Mars during recession in 2004–2006 by the OMEGA visible/near-infrared imaging spectrometer on board Mars Express. *J. Geophys. Res.*, 112, E08S12, doi:10.1029/2006JE002841.

Larson, H. H., and U. Fink (1972), Identification of carbon dioxide frost on the Martian polar caps. *The Astrophysical Journal*, 171, L91.

Leighton, R. B., and B. C. Murray (1966), Behavior of carbon dioxide and other volatiles on Mars. *Science*, 153(3732), 136-144.

Libois, Q., G. Picard, J. L. France, L. Arnaud, M. Dumont, C. M. Carmagnola, and M. D. King (2013) Influence of grain shape on light penetration in snow, *The Cryosphere*, 7, 1803-1818, doi:10.5194/tc-7-1803-2013.

Montmessin, F., and F. Lefèvre (2013), Transport-driven formation of a polar ozone layer on Mars. *Nature geoscience*, 6(11), 930-933, doi:10.1038/ngeo1957.

Quirico, E., and B. Schmitt, (1997), Near-infrared spectroscopy of simple hydrocarbons and carbon oxides diluted in solid N<sub>2</sub> and as pure ices: Implications for Triton and Pluto, *Icarus*, 127(2), 354-378, doi:10.1006/icar.1996.5663.

Räisänen, P., A. Kokhanovsky, G. Guyot, O. Jourdan, and T. Nousiainen (2015), Parameterization of single-scattering properties of snow, *The Cryosphere*, 9, 1277-1301, doi:10.5194/tc-9-1277-2015.

Sokolik, I. N., and O. B. Toon (1999), Incorporation of mineralogical composition into models of the radiative properties of mineral aerosol from UV to IR wavelengths, *J. Geophys. Res.*, 104(D8), 9423–9444, doi:10.1029/1998JD200048.

Stroncik, N. A., and H. U. Schmincke (2002), Palagonite—a review. *International Journal of Earth Sciences*, 91(4), 680-697.

Tillman, J. L., N. C. Johnson, P. Guttorp, and D. B. Percival (1993), The martian annual atmospheric pressure cycle: Years without great dust storms. *Journal of Geophysical Research: Planets* (1991–2012), 98(E6), 10963-10971.

Toon, O. B., C. P. McKay, T. P. Ackerman, and K. Santhanam (1989), Rapid calculation of radiative heating rates and photodissociation rates in inhomogeneous multiple scattering atmosphere, *J. Geophys. Res.*, 94 (D13), 16287-16301, doi:10.1029/JD094iD13p16287.

Warren, S. G., W. J. Wiscombe, and J. F. Firestone (1990), Spectral albedo and emissivity of CO<sub>2</sub> in Martian polar caps: Model results, *J. Geophys. Res.*, 95(B9), 14717–14741, doi:10.1029/JB095iB09p14717.

Warren, S. G., and R. E. Brandt (2008), Optical constants of ice from the ultraviolet to the microwave: A revised compilation, *J. Geophys. Res.*, 113, D14220, doi:10.1029/2007JD009744.

Wiscombe, W. J., and S. G. Warren (1980), A Model for the Spectral Albedo of Snow. I: Pure Snow. *J. Atmos. Sci.*, 37, 2712–2733, doi:10.1175/1520-0469(1980)037<2712:AMFTSA>2.0.CO;2

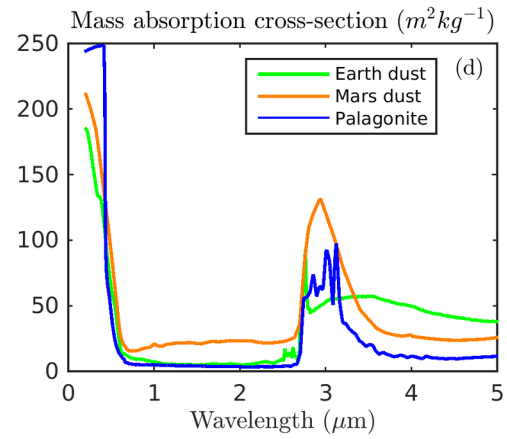
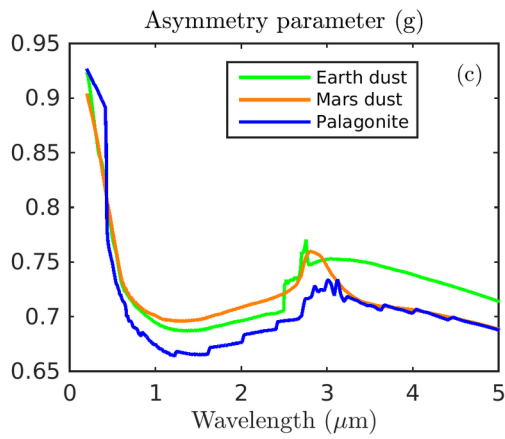
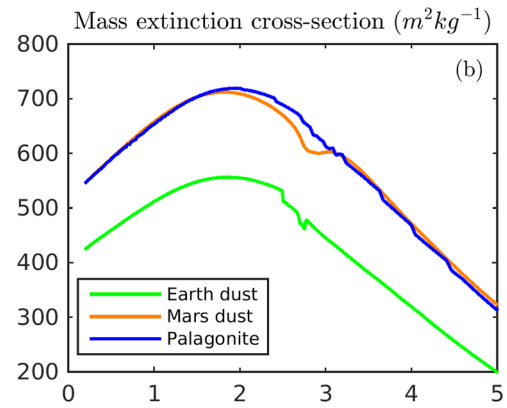
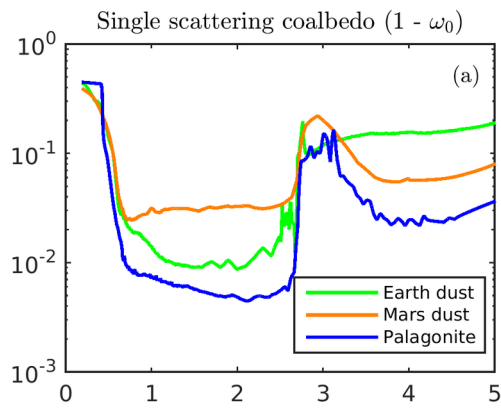
Wolf, M. J., R. T. Clancy, J. D. Goguen, and M. C. Malin, and B. A. Cantor (2010), Ultraviolet dust aerosol properties as observed by MARCI. *Icarus*, 208(1), 143-155.

Wolff, M. J., M. D. Smith, R. T. Clancy, R. Arvidson, M. Kahre, F. Seelos IV, S. Murchie, and H. Savijarvi (2009), Wavelength dependence of dust aerosol single scattering albedo as observed by the Compact Reconnaissance Imaging Spectrometer, *J. Geophys. Res.*, 114, E00D04, doi:10.1029/2009JE003350.

Wolff, M.J., M. D. Smith, R. T. Clancy, N. Spanovich, B. A. Whitney, M. T. Lemmon, J. L. Bandfield, D. Banfield, A. Ghosh, G. Landis, P. R. Christensen, J. F. Bell III and S. W. Squyres (2006), Constraints on dust aerosols from the Mars Exploration Rovers using MGS overflights and Mini-TES. *J. Geophys. Res.*, 111, E12S17, doi:10.1029/2006JE002786.

Author Manuscript

ipt

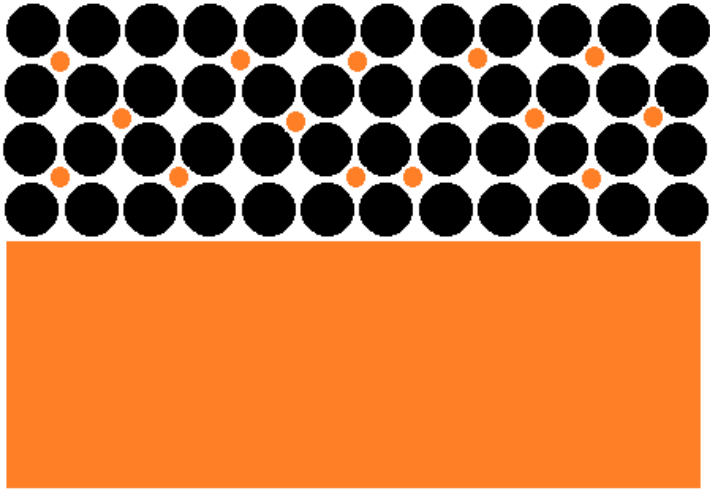


Au

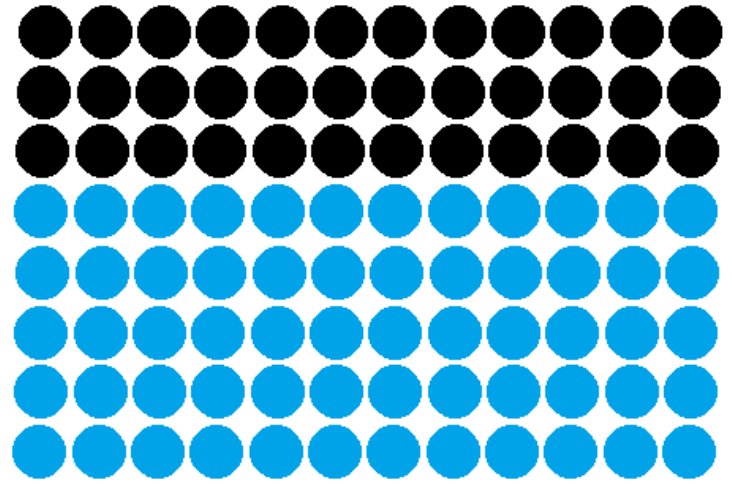
2016JE005040-f01-z-.tif

+

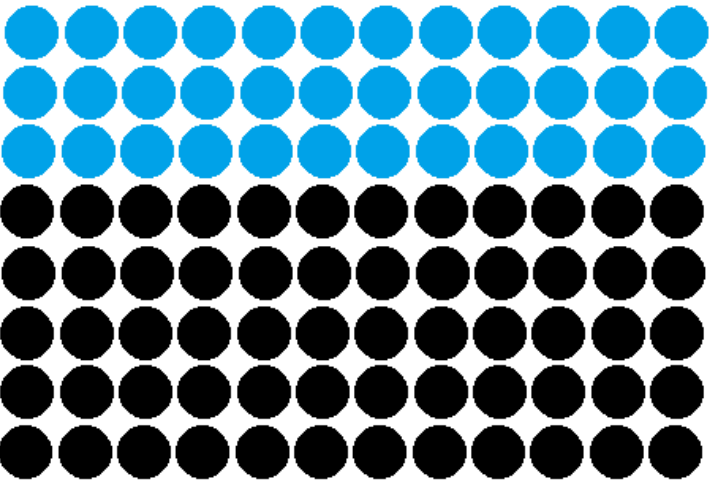
(a)



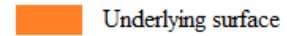
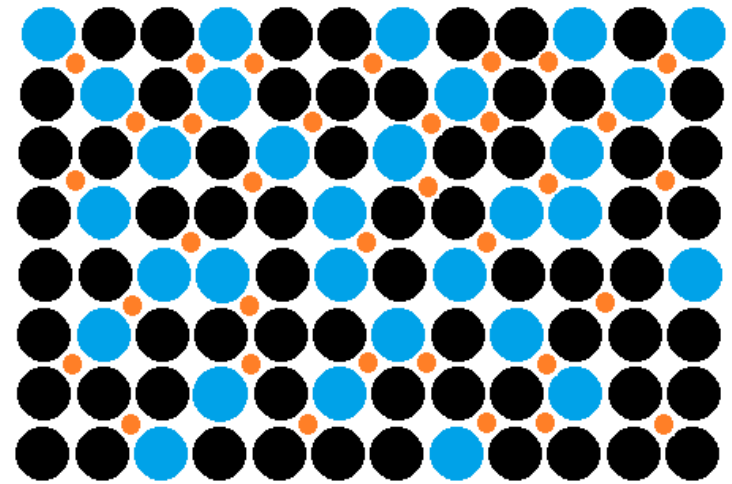
(b)



(c)



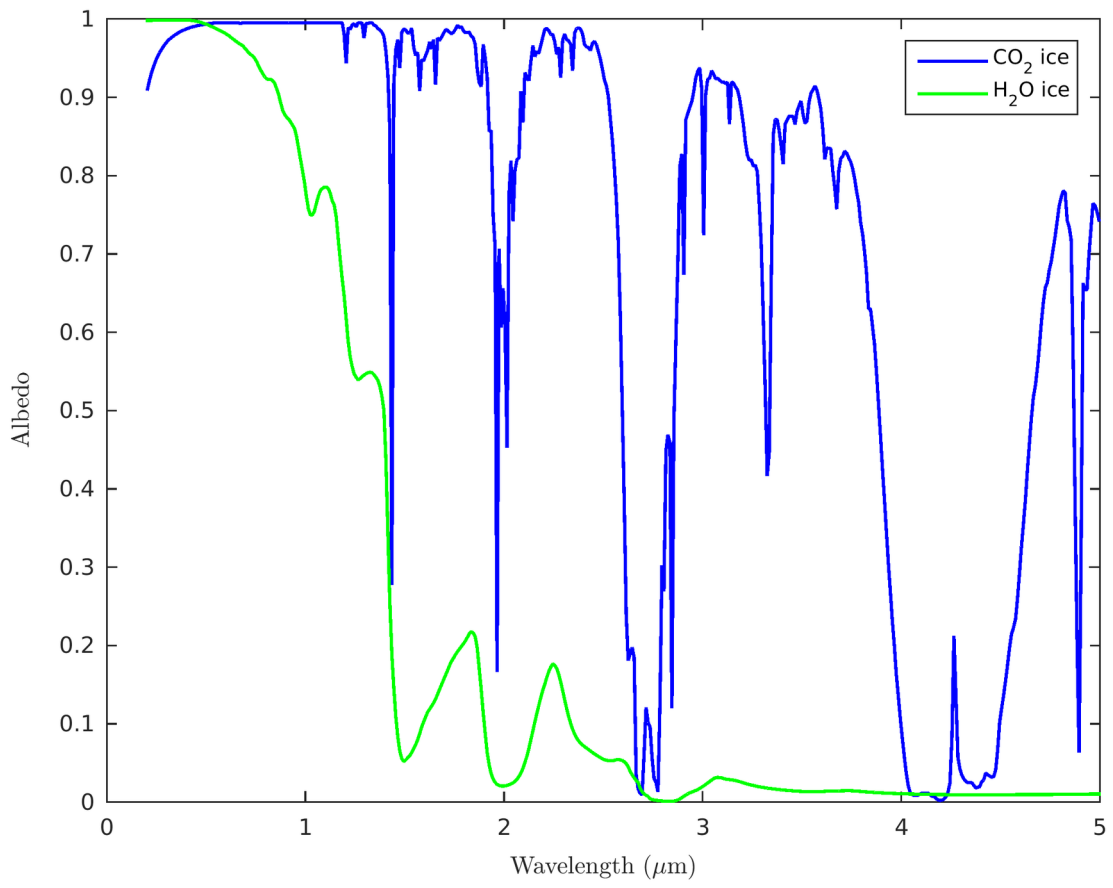
(d)



+

2016JE005040-f02-z-.tif

ipt

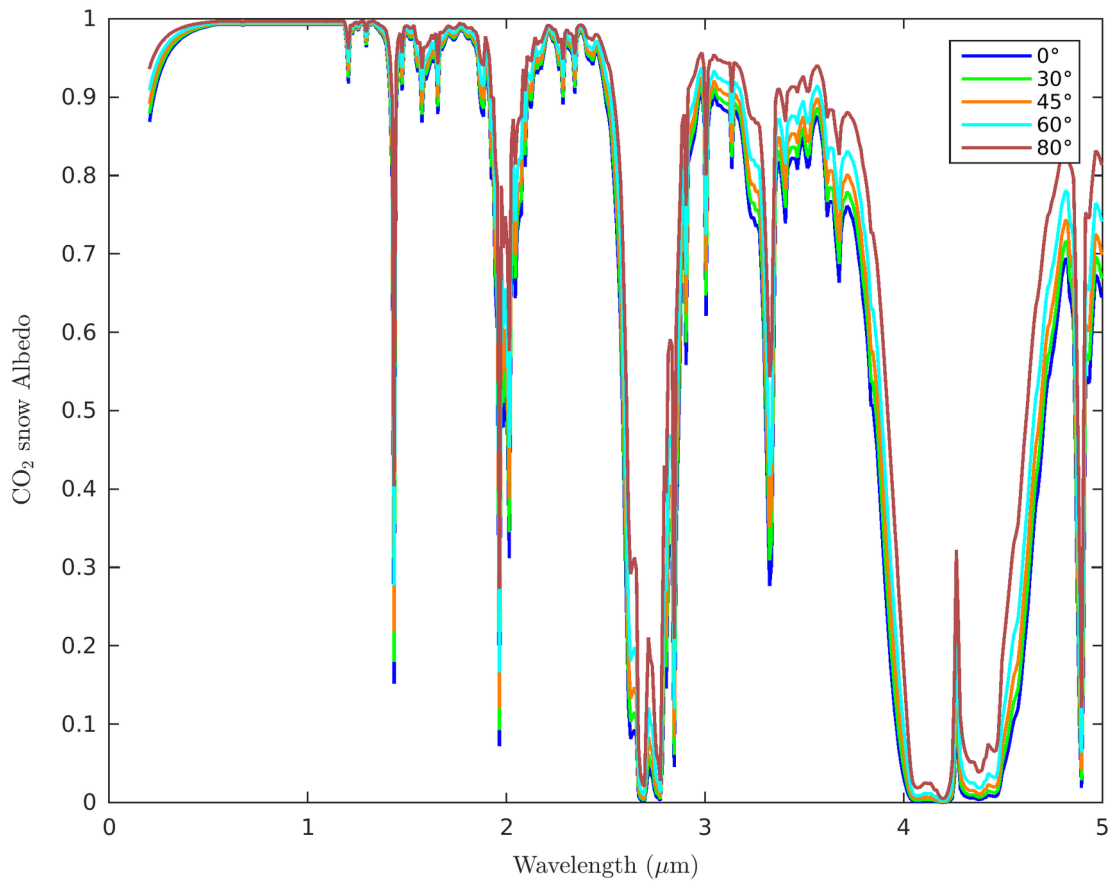


AU

2016JE005040-f03-z-.tif



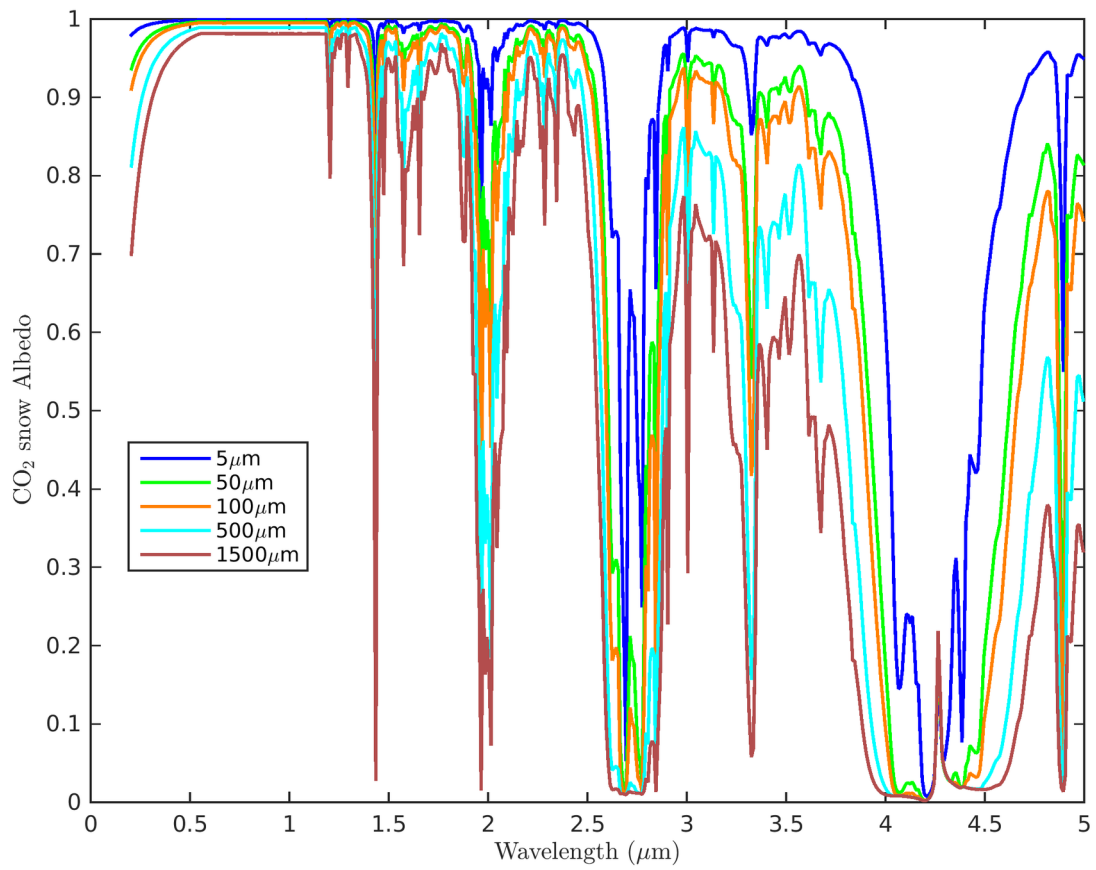
ipt



Au

2016JE005040-f04-z-.tif

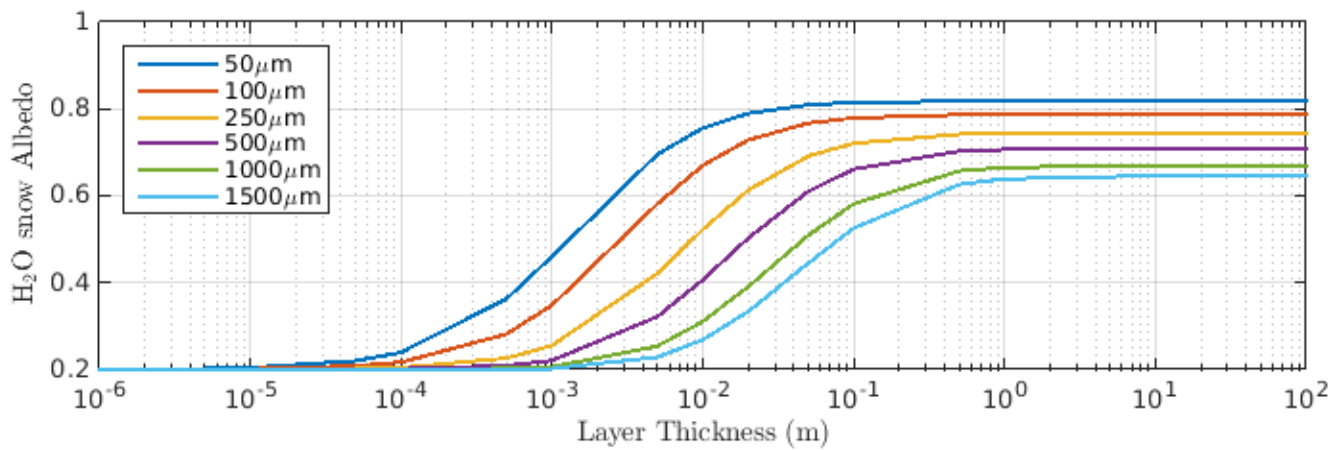
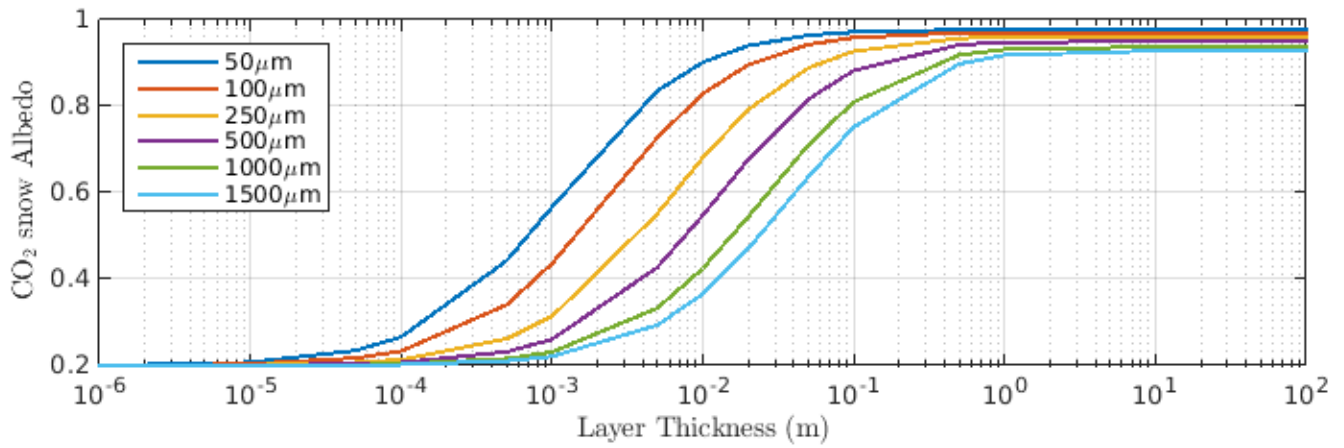
ipt



Au

2016JE005040-f05-z-.tif

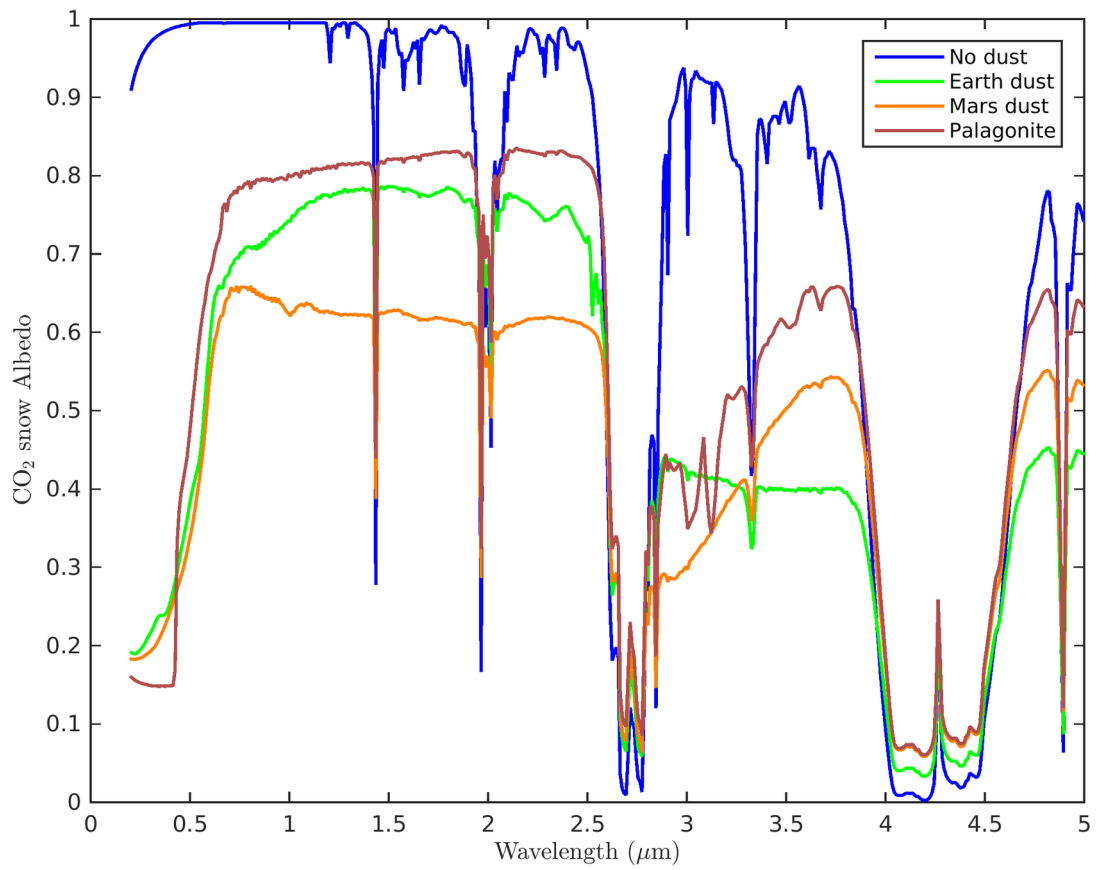
pt



AL

2016JE005040-f06-z-.tif

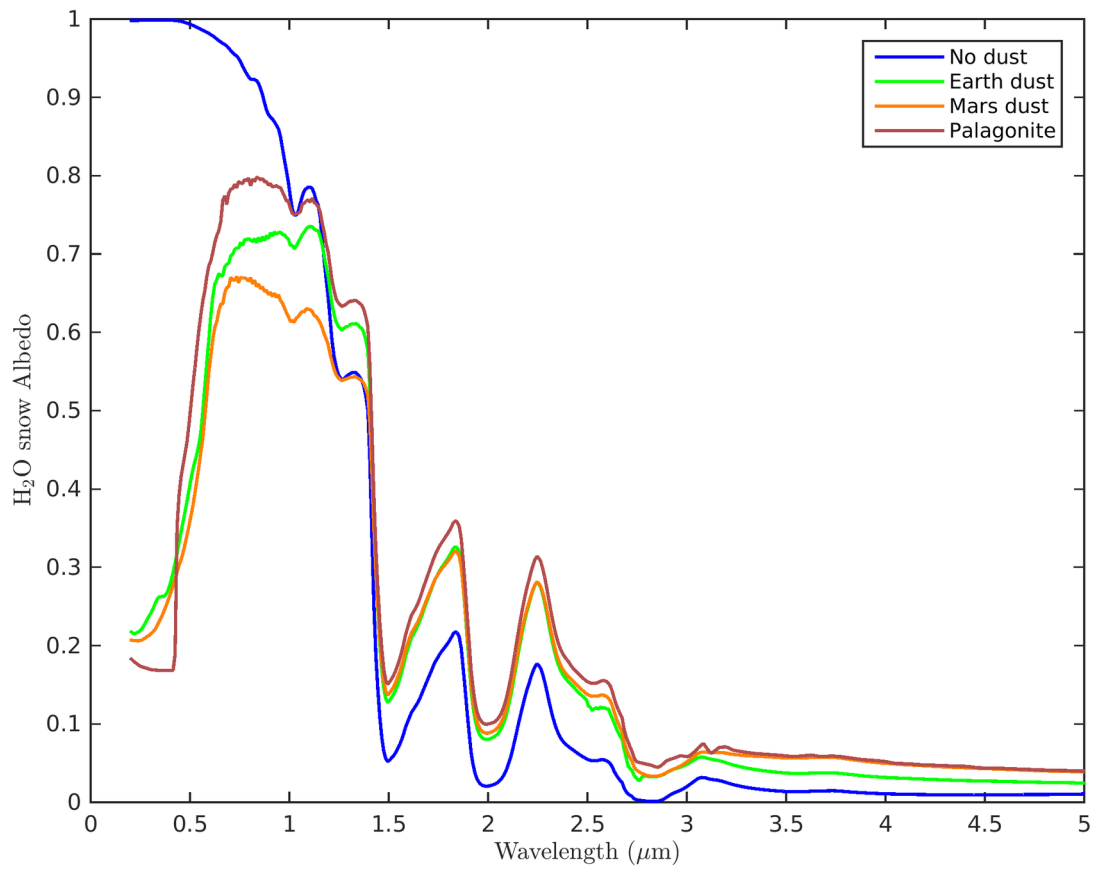
ipt



AU

2016JE005040-f07-z-.tif

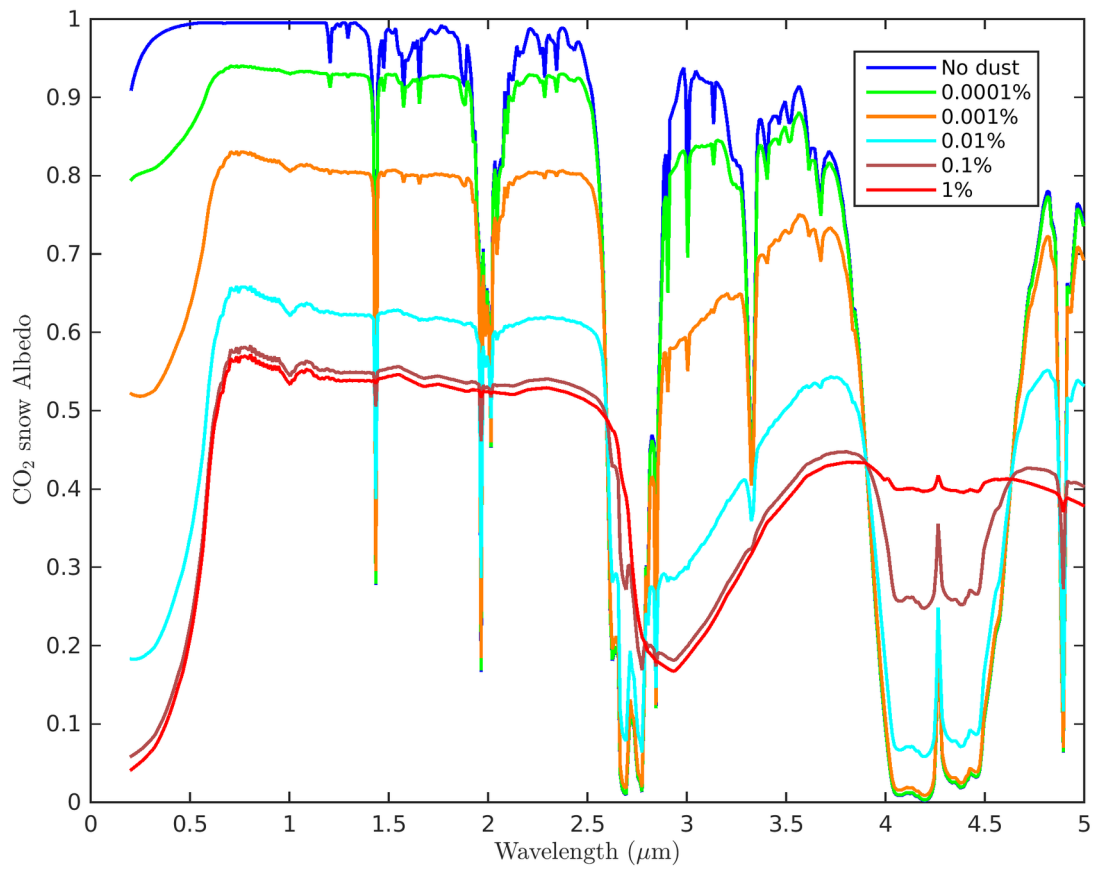
ipt



Au

2016JE005040-f08-z-.tif

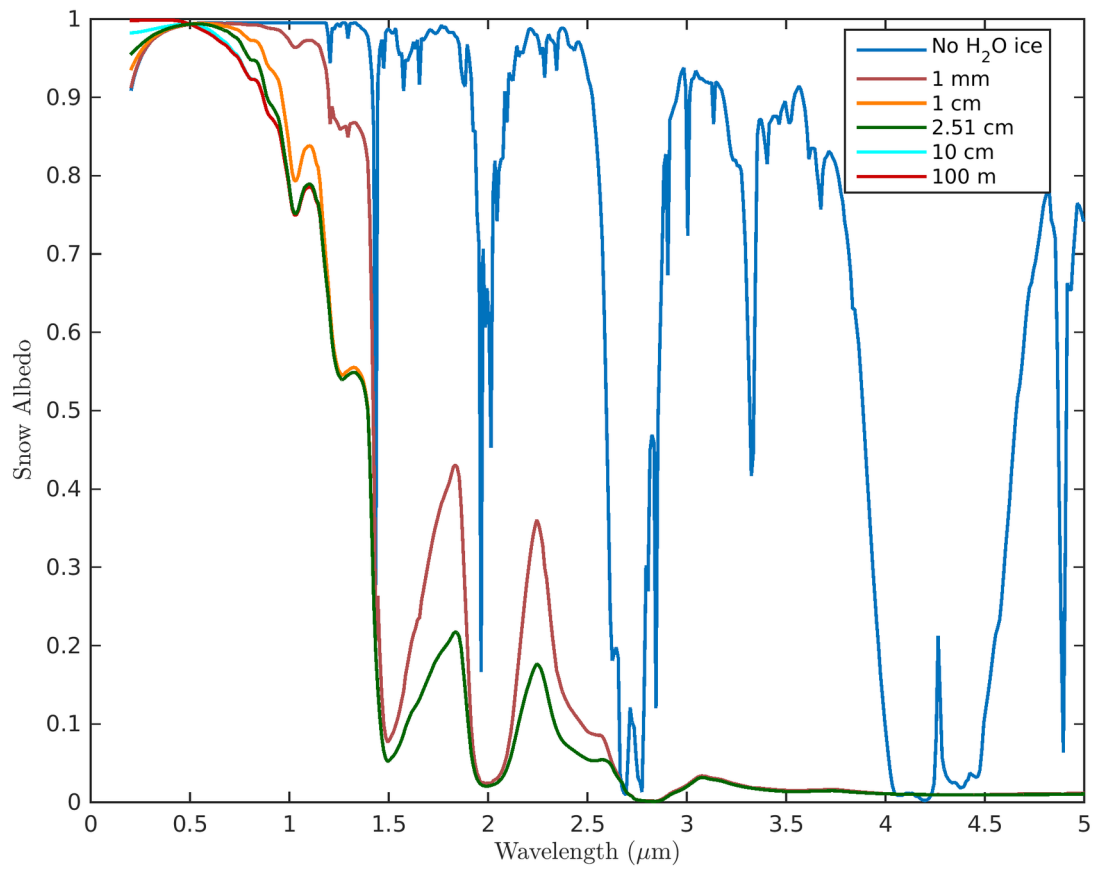
ipt



Au

2016JE005040-f09-z-.tif

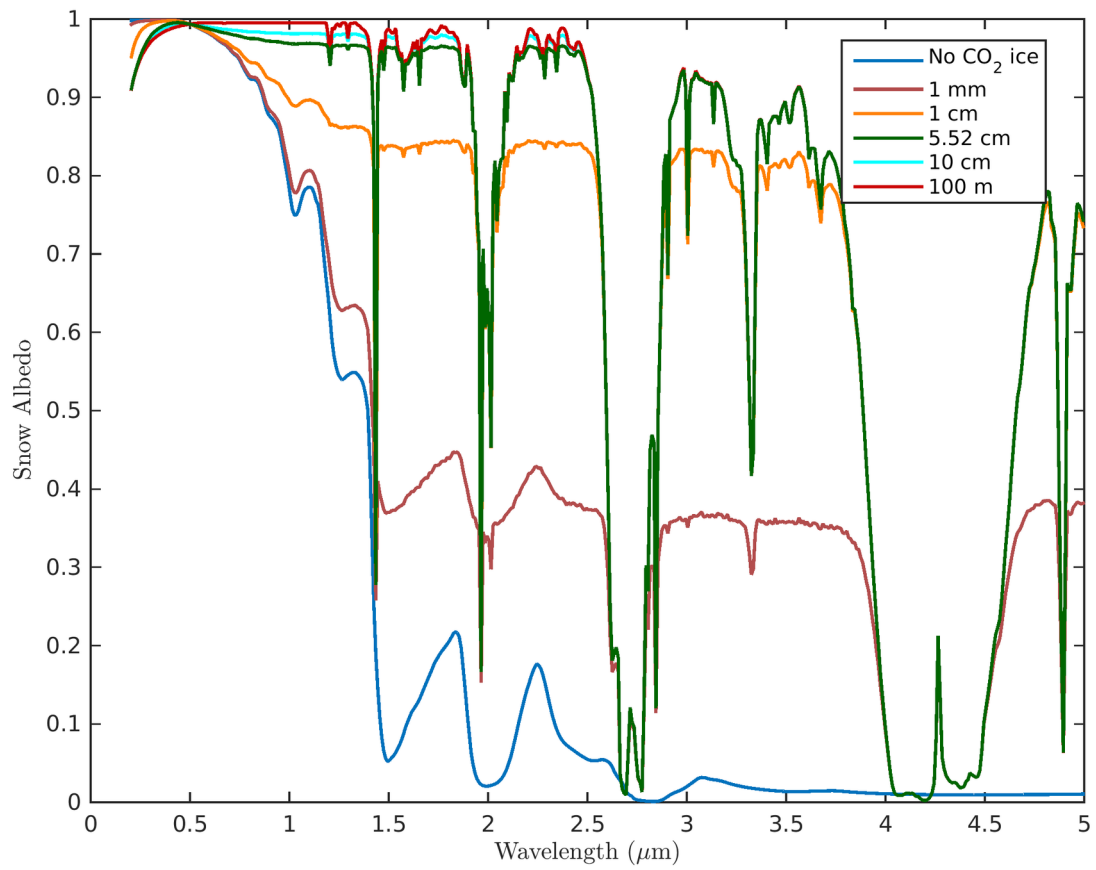
ipt



AU

2016JE005040-f10-z-.tif

ipt

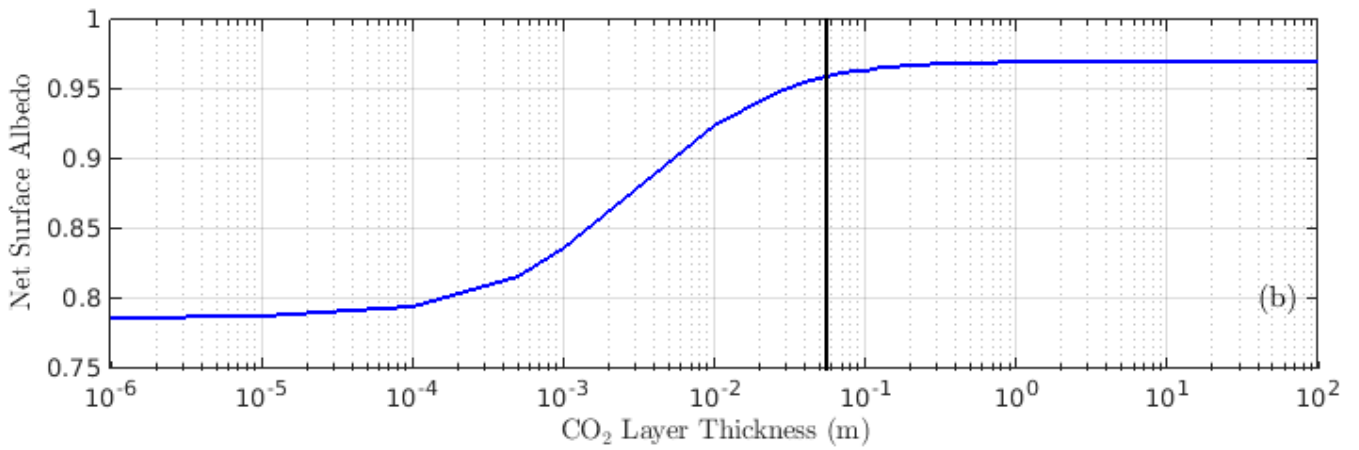
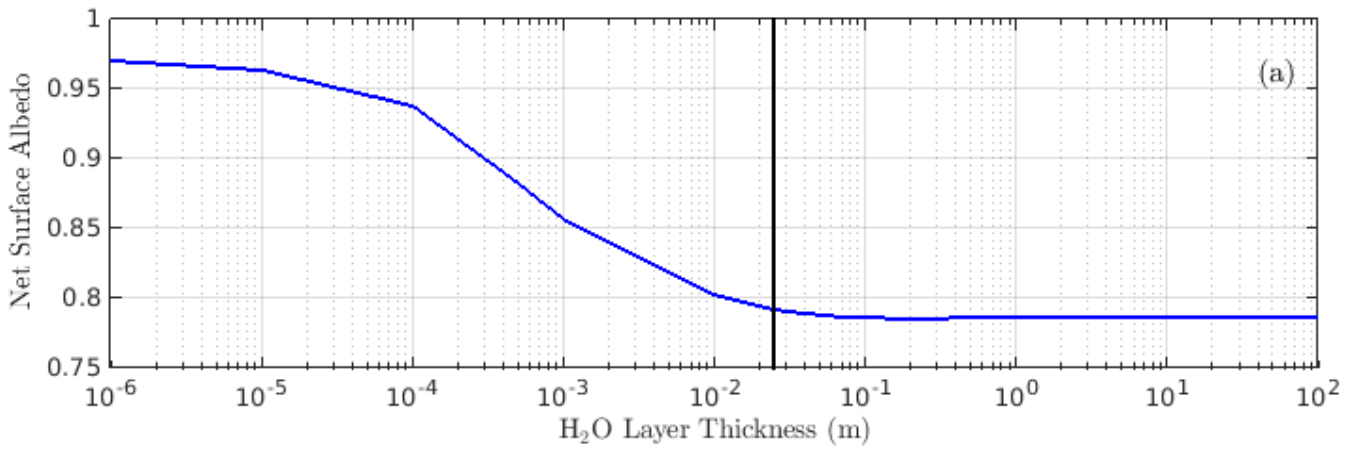


AU

2016JE005040-f11-z-.tif



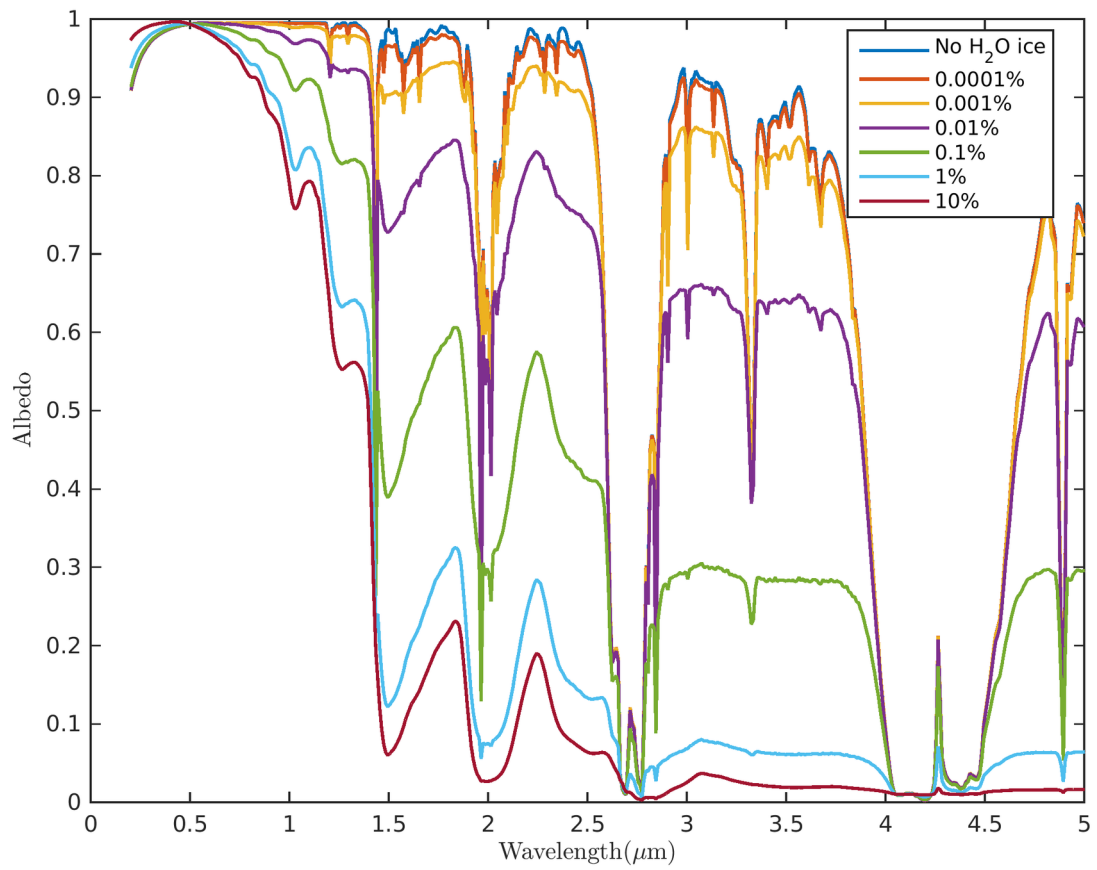
pt



Al

2016JE005040-f12-z-.tif

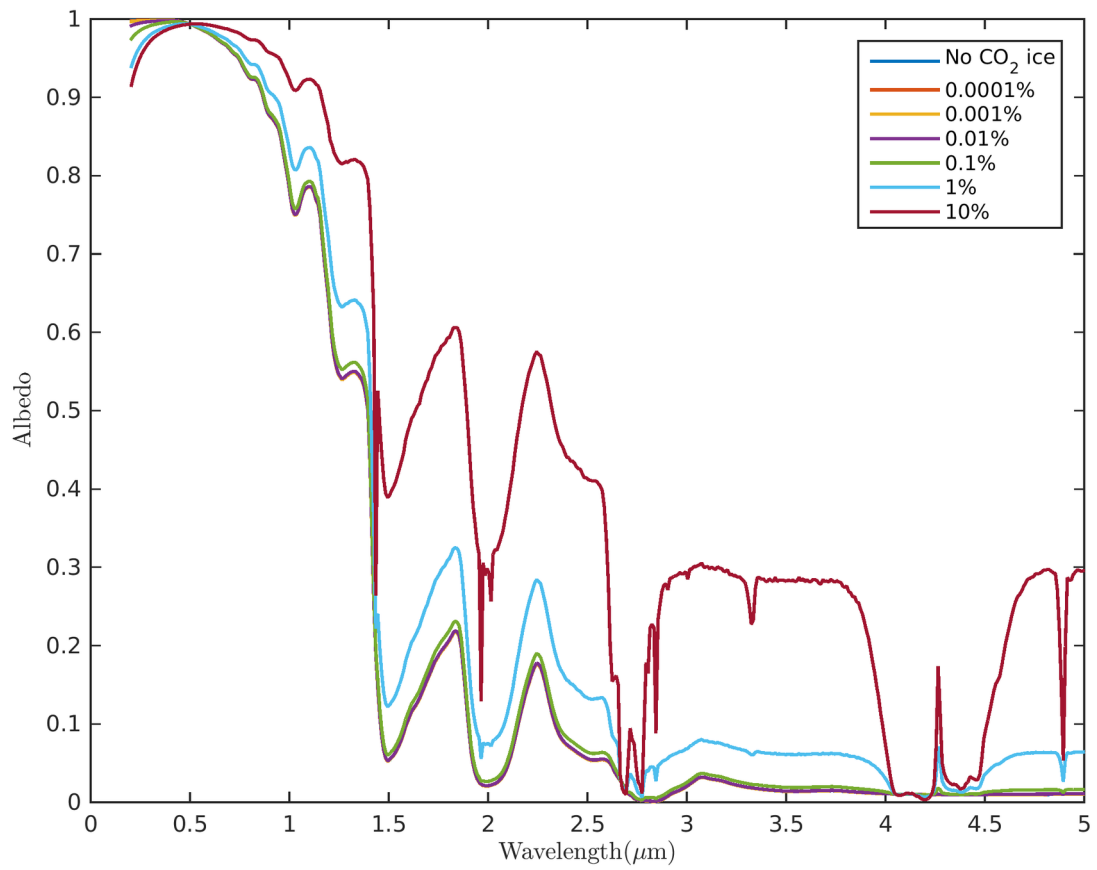
ipt



Au

2016JE005040-f13-z-.tif

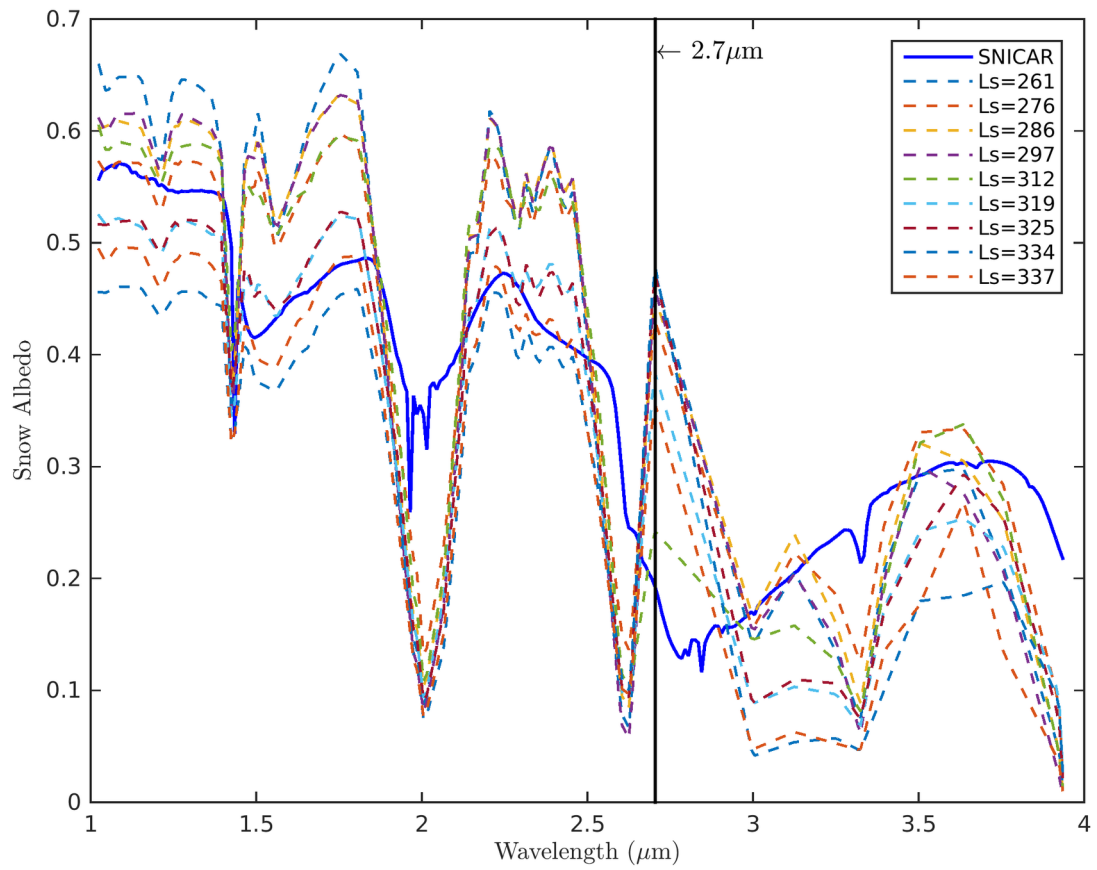
ipt



Au

2016JE005040-f14-z-.tif

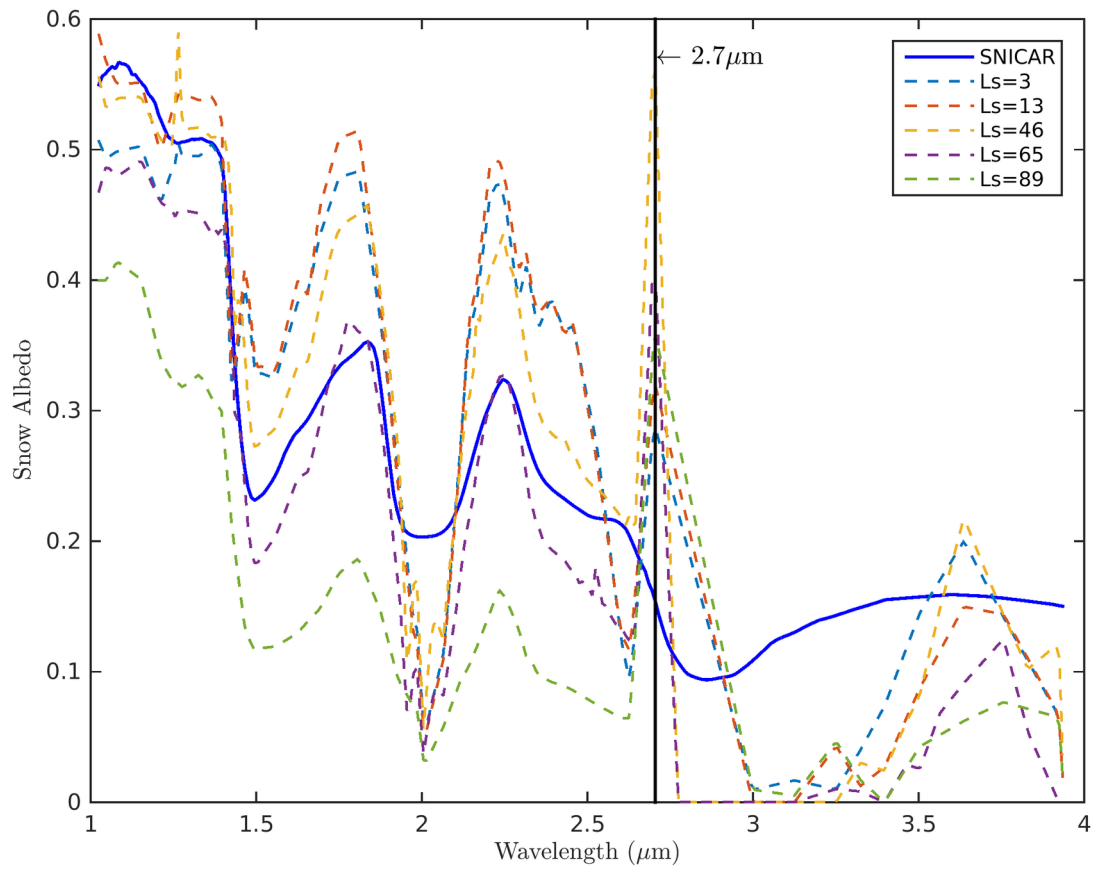
ipt



AU

2016JE005040-f15-z-.tif

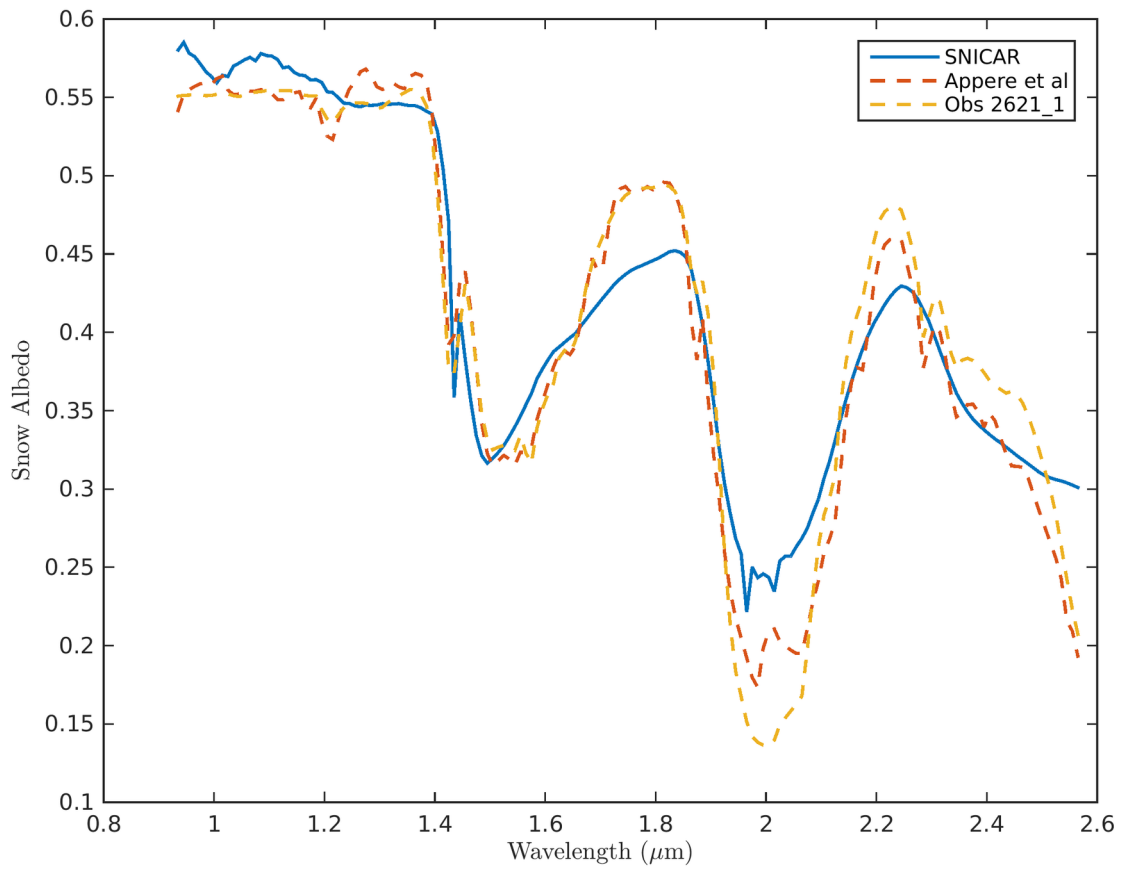
ipt



Au

2016JE005040-f16-z-.tif

ipt



AU

2016JE005040-f17-z-.tif